PHYSICAL REVIEW D **96,** 054513 (2017)

Möbius domain-wall fermions on gradient-flowed dynamical HISQ ensembles

Evan Berkowitz,[1,2] Chris Bouchard,[3,4] Chia Cheng Chang (張家丞),[5] M. A. Clark,[6] Bálint Joó,[7] Thorsten Kurth,[8] Christopher Monahan,[9] Amy Nicholson,[10,5] Kostas Orginos,[4,11] Enrico Rinaldi,[12,2] Pavlos Vranas,[2,5] and André Walker-Loud[5,2]

[1]*Institut für Kernphysik and Institute for Advanced Simulation, Forschungszentrum Jülich, 54245 Jülich, Germany*
[2]*Nuclear and Chemical Sciences Division, Lawrence Livermore National Laboratory, Livermore, California 94550, USA*
[3]*School of Physics and Astronomy, University of Glasgow, Glasgow G12 8QQ, United Kingdom*
[4]*Department of Physics, The College of William & Mary, Williamsburg, Virginia 23187, USA*
[5]*Nuclear Science Division, Lawrence Berkeley National Laboratory, Berkeley, California 94720, USA*
[6]*NVIDIA Corporation, 2701 San Tomas Expressway, Santa Clara, California 95050, USA*
[7]*Scientific Computing Group, Thomas Jefferson National Accelerator Facility, Newport News, Virginia 23606, USA*
[8]*NERSC, Lawrence Berkeley National Laboratory, Berkeley, California 94720, USA*
[9]*New High Energy Theory Center and Department of Physics and Astronomy, Rutgers, The State University of New Jersey, Piscataway, New Jersey 08854, USA*
[10]*Department of Physics, University of California, Berkeley, California 94720, USA*
[11]*Theory Center, Thomas Jefferson National Accelerator Facility, Newport News, Virginia 23606, USA*
[12]*RIKEN-BNL Research Center, Brookhaven National Laboratory, Upton, New York 11973, USA*
(Received 16 February 2017; revised manuscript received 17 August 2017; published 25 September 2017)

We report on salient features of a mixed lattice QCD action using valence Möbius domain-wall fermions solved on the dynamical $N_f = 2 + 1 + 1$ highly improved staggered quark sea-quark ensembles generated by the MILC Collaboration. The approximate chiral symmetry properties of the valence fermions are shown to be significantly improved by utilizing the gradient-flow scheme to first smear the highly improved staggered quark configurations. The greater numerical cost of the Möbius domain-wall inversions is mitigated by the highly efficient QUDA library optimized for NVIDIA GPU accelerated compute nodes. We have created an interface to this optimized QUDA solver in Chroma. We provide tuned parameters of the action and performance of QUDA using ensembles with the lattice spacings $a \simeq \{0.15, 0.12, 0.09\}$ fm and pion masses $m_\pi \simeq \{310, 220, 130\}$ MeV. We have additionally generated two new ensembles with $a \sim 0.12$ fm and $m_\pi \sim \{400, 350\}$ MeV. With a fixed flow time of $t_{gf} = 1$ in lattice units, the residual chiral symmetry breaking of the valence fermions is kept below 10% of the light quark mass on all ensembles, $m_{\text{res}} \lesssim 0.1 \times m_l$, with moderate values of the fifth dimension L_5 and a domain-wall height $M_5 \leq 1.3$. As a benchmark calculation, we perform a continuum, infinite volume, physical pion and kaon mass extrapolation of $F_{K^\pm}/F_{\pi^\pm}$ and demonstrate our results are independent of flow time and consistent with the FLAG determination of this quantity at the level of less than one standard deviation.

DOI: 10.1103/PhysRevD.96.054513

I. INTRODUCTION

QCD [1,2] is the fundamental theory of the strong interaction and one of the three gauge theories of the Standard Model of particle physics. QCD encodes the interactions between quarks and gluons, the constituents of strongly interacting matter, which both carry *color charges* of QCD. At short distances, the quarks and gluons perturbatively interact with a coupling strength that runs to zero in the UV limit [3,4]. Conversely, at long distance/low energy, the IR regime, the coupling becomes $\mathcal{O}(1)$, and QCD becomes a strongly coupled theory. Consequently, the quarks and gluons are confined into the *colorless* hadrons we observe in nature, such as the proton, neutron, pions, etc. In order to compute properties of nucleons, nuclei, and other strongly interacting matter directly from QCD, we must therefore use a nonperturbative regularization scheme.

Asymptotic freedom, the property in which the gauge coupling becomes perturbative in the UV, makes the theory perfectly amenable to a numerical approach. QCD can be constructed on a discrete, Euclidean spacetime lattice, with a technique known as lattice QCD (LQCD). As the discretization scale is made sufficiently fine and the coupling becomes perturbative, the lattice action can be matched onto the continuum action to a desired order in perturbation theory. To aid the matching, effective field theory (EFT) [5] can be used to perform an expansion of the

lattice action in powers of the discretization scale, typically denoted a, which is referred to as the Symanzik expansion [6,7]. There are many different choices for constructing the discretized action, each of which corresponds to a different lattice action. As the continuum limit is taken, the difference between these lattice actions vanishes as the only dimension-4 operators allowed by the symmetries are those of QCD; the discretization effects, which include Lorentz violating interactions, are all described by *irrelevant* operators in the Symanzik expansion. An important test of this universality is to perform calculations of various physical quantities, with different lattice actions, and show consistency between them in the continuum limit. This is now routinely done for mesonic quantities and reviewed every two to three years by the FLAG Working Group, with the latest review in Ref. [8].

Lattice gauge theory began with the formulation of gauge fields on a spacetime lattice as originally proposed by Wilson [9]. The inclusion of fermions presents further challenges. The *naive* discretization of the fermion action leads to the fermion doubling problem, in which there are 2^D fermions in D dimensions for each fermion field implemented. These doublers arise from the periodicity of the lattice action in momentum space and the single derivative in the Dirac equation. Wilson proposed the original method, now known as the Wilson fermion action, to remove these doublers by adding an irrelevant operator to the action which provides an additive mass to the doublers which scales as $1/a$. This irrelevant operator breaks chiral symmetry and requires fine-tuning the bare fermion mass to simulate a theory with light fermions, such as QCD with light *up* and *down* quarks. Despite (or because of) its simplicity, the Wilson fermion action is still one of the most popular in use. These days, the leading $\mathcal{O}(a)$ discretization corrections are removed perturbatively or nonperturbatively through an additional dimension-5 operator, the clover operator $c_{SW}a\bar{q}\sigma_{\mu\nu}G_{\mu\nu}q$, in what is known as the Wilson-Clover or *Clover* fermion action. The parameter c_{SW} is the Sheikholeslami-Wohlert coefficient [10], which can be tuned to remove the $\mathcal{O}(a)$ discretization effects from correlation functions. The idea has also been extended to twisted mass Wilson fermions [11], in which a complex quark-mass term is used, allowing for automatic $\mathcal{O}(a)$ improvement of physical observables provided the theory is computed at *maximal twist* [12].

Another common lattice action is known as the Kogut-Susskind or *staggered* fermion action [13,14]. This action reduces the number of fermion doublers by exploiting a symmetry of the naive fermion action. A suitable spacetime-dependent phase rotation of the fermion fields allows for the Dirac equation to be diagonalized, thereby reducing the number of doublers from 16 to 4, in four spacetime dimensions. To perform numerical simulations with just one or two light fermion flavors, a fourth or square root of the fermion determinant is used [15]. This rooting leads to nonlocal interactions at finite lattice spacing [16–18]; however, perturbation theory [19,20], the renormalization group [21–23], and numerical simulations [24–26] have been used to argue that these nonlocal effects vanish in the continuum limit. While this has not been proven nonperturbatively, some of the potential sicknesses of the theory can be shown to be the same as those of *partially quenched* lattice QCD [27], which we will discuss briefly in short order. While not universally accepted, all numerical evidence suggests that rooted-staggered LQCD is in the same universality class as QCD as the continuum limit is taken [8,28–30].

Determining a nonperturbative regulator that both preserves chiral symmetry and has the correct number of light degrees of freedom is challenging. It has been shown that in four spacetime dimensions, one cannot simultaneously have all four of the conditions: chiral symmetry, ultralocal action, undoubled fermions, and the correct continuum limit. This is known as the Nielsen-Ninomiya no-go theorem [31–33]. However, one can extend the definition of chiral symmetry at finite lattice spacing: if the lattice Dirac operator, D, satisfies the Ginsparg-Wilson relation [34]

$$\{\gamma_5, D\} = aD\gamma_5 D, \tag{1}$$

it will respect chiral symmetry even at finite lattice spacing [35]. One consequence is the theory will be automatically $\mathcal{O}(a)$ improved as the only nontrivial dimension-5 operator that cannot be removed through field redefinitions and equations of motion is the clover operator, which explicitly breaks chiral symmetry and is thus not allowed. There are two lattice actions which satisfy the Ginsparg-Wilson relation: the domain-wall (DW) fermion action [36–38] and the overlap fermion action [39–41]. The DW fermion action is formulated with a finite fifth dimension of extent L_5, where the left and right chiral modes are bound to opposite ends of the fifth dimension. The gluon action is a trivial copy of the four-dimensional (4D) action on each fifth-dimensional slice with unit link variable between the slices, and so the fermions have only a simple kinetic action in the fifth dimension. At finite L_5, the left and right modes have a nonvanishing overlap due to fermion modes which propagate into the fifth dimension. The massive modes decay exponentially in the fifth dimension, while the fermion zero modes have only a power-law falloff. This small overlap leads to a small, residual breaking of chiral symmetry at finite L_5, characterized by a quantity known as m_{res}. The overlap fermion action can be shown to be equivalent to the domain-wall action as $L_5 \to \infty$ [42,43] and respects chiral symmetry to a desired numerical precision.

The numerical cost of generating lattice ensembles with domain-wall and overlap actions is 1 or more orders of magnitude greater than the cost of generating ensembles with Wilson-type or staggered fermion actions [44]. This has led to interest in, and the development of, mixed lattice

actions or mixed-actions (MA) [45], in which the valence and sea-quark lattice actions are not the same at finite lattice spacing. In the most common MALQCD calculations, the dynamical sea-quark action is generated with a numerically less expensive discretization scheme, such as staggered- or Wilson-type fermions, while the valence-quark action, which is used to construct correlation functions, is implemented with domain-wall or overlap fermions, thus retaining the full chiral symmetry in the valence sector. The first implementation of a MALQCD calculation was performed by the Lattice Hadron Physics Collaboration [46] utilizing DW fermions on the publicly available asqtad (a^2 tadpole improved) [47,48] rooted staggered ensembles generated by the MILC Collaboration [30,49]. A number of important results were obtained with this particular MALQCD setup, including the first dynamical calculation of the nucleon axial charge with light pion masses [50] and more general nucleon structure [51,52], the first dynamical calculation of two-nucleon elastic scattering [53], a precise calculation of the $I = 2\pi\pi$ scattering length [54], a detailed study of the quark-mass dependence of the light baryon spectrum [55], a calculation of the kaon bag parameter with fully controlled uncertainties [56], and many more.

The predominant reason for the success of these MALQCD calculations is the good chiral symmetry properties of the DW action, which significantly suppresses chiral symmetry breaking from the staggered sea fermions and discretization effects. EFT can be used to understand the salient features of such MALQCD calculations. Chiral perturbation theory (χPT) [57–59] can be extended to incorporate discretization effects into the analytic formulas describing the quark-mass dependence of various hadronic quantities. The procedure is to first construct the local Symanzik action for a given lattice action and then to use spurion analysis to construct all operators in the low-energy EFT describing such a lattice action, including contributions from higher-dimension operators [60]. The MA EFT [61] for DW valence fermions on dynamical rooted staggered fermions is well developed [62–69]. The use of valence fermions which respect chiral symmetry leads to a universal form of the MA EFT extrapolation formulas at next-to-leading order (NLO) in the dual quark-mass and lattice spacing expansions [65,68]. This universal behavior follows from the suppression of chiral symmetry breaking discretization effects from the sea sector when constructing correlation functions from valence fermions. Further, quantities which are protected by chiral symmetry are free of new low-energy constants (LECs) at NLO provided on-shell renormalized quantities are used in the extrapolation formulas [64,65]. This universality allows for the derivation of NLO MA EFT formula directly from their partially quenched χPT [70–78] counterparts, provided they are known [79–86]. MALQCD calculations with DW valence quarks on the asqtad rooted staggered ensembles have been stress tested through a comparison of quantities which are directly sensitive to the unitarity violations present in MALQCD calculations, in particular the a_0 meson correlation function [87,88]. There are a few other MA constructions that have been tested but only a few others that are actively used. The HPQCD Collaboration utilizes highly improved staggered quark (HISQ) valence fermions on the asqtad ensembles; for example, see Refs. [89,90]. The χQCD Collaboration utilizes overlap valence fermions on the dynamical $N_f = 2 + 1$ domain-wall ensembles [91–93] generated by the RBC/UKQCD Collaboration [94,95]. The work in Refs. [96–99] uses valence overlap fermions on the $N_f = 2 + 1 + 1$ HISQ ensembles [100]. The PNDME Collaboration has utilized clover improved valence fermions on the $N_f = 2 + 1 + 1$ HISQ ensembles [100,101]. While this MA choice is economical, it does not benefit from the suppression of chiral symmetry breaking discretization effects as with the DW on asqtad or overlap on DW MALQCD calculations.

Given the successes described above, MALQCD provides an economical means of performing LQCD calculations in which chiral symmetry breaking effects are highly suppressed by utilizing a valence fermion action that respects chiral symmetry in combination with a set of LQCD ensembles that do not but are less numerically expensive to generate. In this article, we motivate a new MALQCD action and present numerical evidence for salient features of the action.

II. MÖBIUS DOMAIN-WALL FERMIONS ON GRADIENT-FLOWED HISQ ENSEMBLES

Present-day LQCD calculations for mesonic quantities are performed with multiple lattice spacings, multiple volumes, and physical pion masses, allowing for complete control over all LQCD systematics; see Ref. [8] for many examples. The simplest single baryon properties are also computed with multiple lattice spacings/volumes and near-physical and sometimes physical pion masses [102–105], including the first calculation of the nucleon axial charge with both physical pion masses and a continuum limit [106] and isospin violating corrections [106–109]. If one is interested in a set of ensembles allowing for this much control over LQCD systematics, there are only two such sets publicly available, both of which are generated and provided by the MILC Collaboration: the $N_f = 2 + 1$ asqtad ensembles [30] and the $N_f = 2 + 1 + 1$ HISQ [110] ensembles generated more recently [111,112]. The HISQ ensembles have taste splittings in the pseudoscalar sector that are one generation finer in discretization [112], such that the $a \sim 0.15$ fm HISQ ensemble taste violations are similar in size to the $a \sim 0.12$ fm asqtad ensembles. There is a vast set of HISQ ensembles with $130 \lesssim m_\pi \lesssim 310$ MeV, strange and charm quark masses tuned near their physical values and lattice spacings of $a \sim \{0.15, 0.12, 0.09, 0.06, 0.042, 0.03\}$ fm, including

TABLE I. The HISQ ensembles used in this work and planned for future MALQCD calculations. In addition to the pion mass and lattice spacing, we list the number of configurations used in the present work, N_{cfg} as well as the Monte Carlo time, $\Delta\tau_{MC}$, by which the configurations were separated in this work. The short name, introduced in Ref. [101], is for brevity. The last two HISQ ensembles were generated at LLNL targeting heavier pion masses to test the radius of convergence of the chiral extrapolation in future MALQCD calculations.

Short name	Ensemble	$am_\pi^{\mathrm{HISQ-5}}$	$am_{ss}^{\mathrm{HISQ-5}}$	Volume	$\sim a$ (fm)	$\sim m_\pi$ (MeV)	$m_\pi L$	N_{cfg}	$\Delta\tau_{MC}$
a15m310	l1648f211b580m013m065m838a	0.23646(17)	0.51858(17)	$16^3 \times 48$	0.15	310	3.78	196	50
a12m310	l2464f211b600m0102m0509m635a	0.18931(10)	0.41818(10)	$24^3 \times 64$	0.12	310	4.54	199	25
a09m310	l3296f211b630m0074m037m440e	0.14066(13)	0.31133(12)	$32^3 \times 96$	0.09	310	4.50	196	24
a15m220	l2448f211b580m0064m0640m828a	0.16612(08)	0.51237(10)	$24^3 \times 48$	0.15	220	3.99	199	25
a12m220	l3264f211b600m00507m0507m628a	0.13407(06)	0.41559(07)	$32^3 \times 64$	0.12	220	4.29	199	25
a09m220	l4896f211b630m00363m0363m430a	0.09849(07)	0.30667(07)	$48^3 \times 96$	0.09	220	4.73	⋯	⋯
a15m130	l3248f211b580m00235m0647m831a	0.10161(06)	0.51427(05)	$32^3 \times 48$	0.15	130	3.25	⋯	⋯
a12m130	l4864f211b600m00184m0507m628a	0.08153(04)	0.41475(05)	$48^3 \times 64$	0.12	130	3.91	⋯	⋯
a12m400	l2464f211b600m0170m0509m635a	0.24398(12)	0.41970(12)	$24^3 \times 64$	0.12	400	5.86	⋯	⋯
a12m350	l2464f211b600m0130m0509m635a	0.21376(13)	0.41923(13)	$24^3 \times 64$	0.12	350	5.13	⋯	⋯

multiple spatial volumes and lighter than physical strange quark masses. In addition to the publicly available HISQ ensembles, we have generated two additional sets at $a \sim 0.12$ fm and $m_\pi \approx 350, 400$ MeV with fixed volume in lattice units such that $m_\pi L \geq 5.1$. In Table I, we list the HISQ ensembles utilized in the present work as well as ensembles for which we have tuned the Möbius DW fermion (MDWF) parameters for future work.

Given the great success of the MA DW fermion on asqtad LQCD calculations [50–56], we have chosen to use DW fermions for the present MALQCD calculations as well. In the present work, we have chosen to use the MDWF action [113–115] which offers reduced residual chiral symmetry breaking at fixed fifth-dimensional extent, L_5. With the introduction of two new parameters, b_5 and c_5, the Möbius kernel can be smoothly interpolated between the Shamir [37] and the Neuberger/Boriçi [42,43,116,117] kernels. Following Ref. [115], the Möbius kernel can be expressed as

$$D^{\mathrm{Möbius}}(M_5) = \frac{(b_5 + c_5) D^{\mathrm{Wilson}}(M_5)}{2 + (b_5 - c_5) D^{\mathrm{Wilson}}(M_5)}. \quad (2)$$

Alternatives include a polar decomposition to the sign function [118–120] or other methods of approximating the sign function [121]. In this work, we have always chosen values of b_5 and c_5 with the constraint $b_5 - c_5 = 1$, such that the Möbius kernel is a rescaled version of the Shamir kernel

$$D^{\mathrm{Möbius}}(M_5) = \frac{\alpha D^{\mathrm{Wilson}}(M_5)}{2 + D^{\mathrm{Wilson}}(M_5)} \equiv \alpha D^{\mathrm{Shamir}}(M_5). \quad (3)$$

It was demonstrated in Ref. [115] that this rescaling factor, α, exponentially enhances the suppression of residual chiral symmetry breaking as

$$m_{\mathrm{res}} \sim e^{-\alpha L_5}, \quad (4)$$

provided the action is in a regime where these exponentially damped terms are the dominant contribution to m_{res} and α is not too large, but of the order $\alpha \sim 2$–4. With the constraint $b_5 - c_5 = 1$, the rescaling factor is given by $\alpha = b_5 + c_5$.

III. GRADIENT-FLOW SMEARING

From the DW on asqtad action [122], it is known that the asqtad gauge fields required additional levels of smearing to reduce the residual chiral symmetry breaking. For that action, Hypercubic (HYP) smearing [123–126] was utilized for this purpose. In this work, we choose to investigate the use of the gradient flow [127–129] as a smearing method. The gradient flow is a nonperturbative, classical evolution of the original fields in a new parameter, the *flow time*, that drives those fields toward a classical minimum. In real space, this corresponds to smearing out the degrees of freedom through an infinitesimal *stout-smearing* procedure [130].

Gradient flow smearing introduces a new scale, of the order $l_{gf} \sim \sqrt{8 t_{gf}} a$, where t_{gf} is the (dimensionless) flow time. Correlation functions depend upon this new scale, which can serve as a nonperturbative, rotationally invariant UV regulator that provides the possibility for improved renormalization procedures for various LQCD matrix elements [131–137]. Here, however, we are interested in the gradient flow as a smearing algorithm [138,139].

To ensure that the continuum limit of LQCD matrix elements is free of any flow-time dependence, one must use a fixed flow time in lattice units such that all flow-time dependence extrapolates to zero as the continuum limit is taken.

In this work, we have found that moderate values of the flow time allow for a reduction of the residual chiral symmetry breaking such that $m_{\mathrm{res}} < 0.1 \times m_l^{dwf}$ for moderate

values of L_5. The resulting flow-time dependence of $m_{\rm res}$ at fixed pion mass demonstrates that the gradient flow highly suppresses the zero-mode contributions to $m_{\rm res}$, such that an exponential dependence of $m_{\rm res}$ on L_5 is recovered. Further, we have observed that gradient-flow smearing has allowed us to use small values of the DW height, with $M_5 \leq 1.3$ on all ensembles used in this work. This is important because with the larger values of M_5 used in the DW on asqtad calculations, there was strong contamination of the UV modes with an oscillatory time behavior, modes which are known to decouple as $M_5 \to 1$ [140]. With the values of M_5 used in this work, there is no discernible contamination from these modes at larger flow times.

We finally settled on a gradient flow time of $t_{gf} = 1.0$, which provided significant suppression of residual chiral symmetry breaking without introducing a large flow-time length scale. In the next section, we present detailed calculations showing the flow-time dependence of various quantities. This action has been used to compute the $\pi^- \to \pi^+$ matrix element relevant for neutrinoless double beta decay [141] and also to perform an exploratory calculation of an improved method of computing hadronic matrix elements [142] and an application to g_A [143].

A. Tuning the action

Before showing results, we describe how to match the valence MDWF action and the HISQ action. With a given flow time, our general algorithm for choosing values of the MDWF action parameters is:

(i) For a fixed value of L_5, optimize M_5 to minimize the resulting value of $m_{\rm res}$.
(ii) Vary the values of L_5, b_5, and c_5 under the constraints $b_5 - c_5 = 1$ and $m_{\rm res} \leq 0.1 m_l^{dwf}$ while minimizing L_5.
(iii) Tune m_l^{dwf} and m_s^{dwf} such that $m_\pi^{dwf} \simeq m_\pi^{\text{HISQ-5}}$ and $m_{ss}^{dwf} \simeq m_{ss}^{\text{HISQ-5}}$ within $\mathcal{O}(2\%)$ or less where HISQ-5 denotes the taste-5 pseudoscalar mass of the dynamical HISQ action and m_{ss} is the mass of the connected $\bar{s}\gamma_5 s$ pseudoscalar meson.

This procedure required just a few iterations to converge to the desired results. For this work, we have used the definition of $m_{\rm res}$ from the Shamir kernel as the residual chiral symmetry breaking between Shamir and Möbius becomes the same in the continuum limit [115],

$$m_{\rm res}(t) = \frac{\sum_{\mathbf{x}} \langle \bar{Q}(t,\mathbf{x})\gamma_5 Q(t,\mathbf{x}) \bar{q}(0,\mathbf{0})\gamma_5 q(0,\mathbf{0}))\rangle}{\sum_{\mathbf{x}} \langle \bar{q}(t,\mathbf{x})\gamma_5 q(t,\mathbf{x}) \bar{q}(0,\mathbf{0})\gamma_5 q(0,\mathbf{0}))\rangle}, \quad (5)$$

where Q is a quark field in the midpoint of the fifth dimension and q is a quark field bound to the domain wall.

In Table II, we list the resulting MDWF parameters at the chosen gradient flow time of $t_{gf} = 1$. These parameters were used in Refs. [141,143].

TABLE II. Tuned MDWF parameters for our MALQCD calculations. Some of the ensembles are used, for example, in Refs. [141,143].

Ensemble	M_5	L_5	b_5	c_5	t_{gf}	am_l^{mdwf}	am_s^{mdwf}
a12m400	1.2	8	1.25	0.25	1.0	0.02190	0.0693
a12m350	1.2	8	1.25	0.25	1.0	0.01660	0.0693
a15m310	1.3	12	1.50	0.50	1.0	0.01580	0.0902
a12m310	1.2	8	1.25	0.25	1.0	0.01260	0.0693
a09m310	1.1	6	1.25	0.25	1.0	0.00951	0.0491
a15m220	1.3	16	1.75	0.75	1.0	0.00712	0.0902
a12m220	1.2	12	1.50	0.50	1.0	0.00600	0.0693
a09m220	1.1	8	1.25	0.25	1.0	0.00449	0.0491
a15m130	1.3	24	2.25	1.25	1.0	0.00216	0.0902
a12m130	1.2	20	2.00	1.00	1.0	0.00195	0.0693

IV. FLOW TIME DEPENDENCE OF VARIOUS QUANTITIES

To study the efficacy of this action, we compute the flow-time dependence of various quantities. In the next section, we will show that the continuum limits of various ratios of physical quantities are flow-time independent. In order to test the flow-time dependence, we tune the input quark masses to hold the pion mass and the connected ss pseudoscalar meson masses fixed within $\mathcal{O}(2\%)$. In the Appendix (Table VII), we list the tuned values of the input quark masses for various flow times on the ensembles used in this work. We also list the resulting values of the plaquette, $m_{\rm res}$, and the values of Z_A determined as described below. In Fig. 1, we show the effective masses of the pion and nucleon, respectively, on the a15m310 ensemble for all flow times. We observe that the contamination from oscillatory modes is suppressed at larger flow times.

From the input quark masses used at fixed pseudoscalar masses, and the average values of the plaquettes, one observes a substantial flow-time dependence of UV quantities. This is expected as the gradient flow smearing filters out the UV modes of the gauge fields. It is important to check the flow-time dependence of hadronic quantities and verify the continuum limit is flow-time independent. This can easily be checked with ratios of hadronic quantities. In Table VIII, we list values of the meson masses m_π, m_K, and m_{ss} as well as the decay constants F_π and F_K and the nucleon mass m_N. We also provide the ratios of F_K/F_π and m_N/F_π.

A. Fit functions

To determine the value of $m_{\rm res}$, we fit the correlation function described by Eq. (5) to a constant.

The meson correlation functions were folded in time to double the statistics while the nucleon correlation functions were averaged between the forward propagating positive parity interpolating operator and the backward propagating

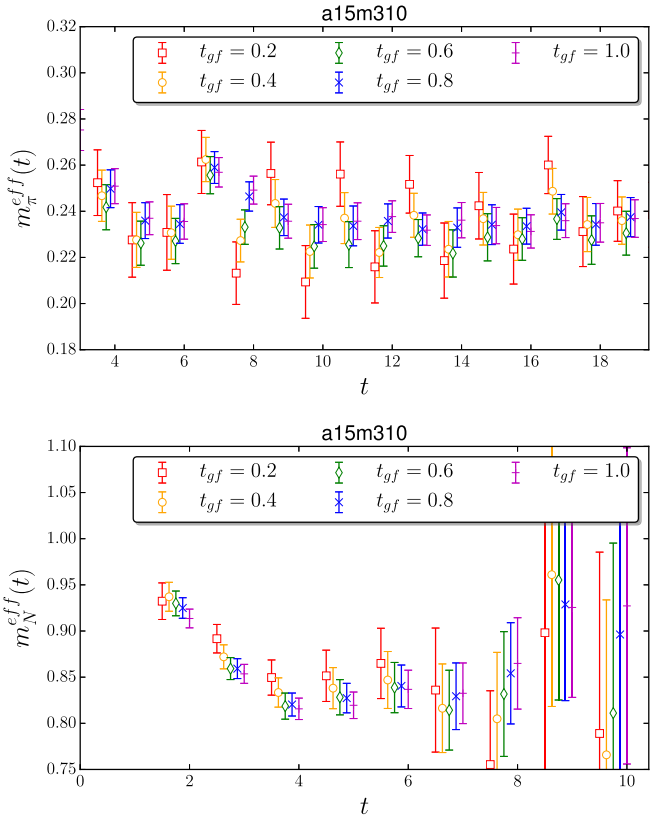

FIG. 1. Effective mass of the pion (top) and proton (bottom) as a function of the Euclidean time t, at different flow times on the a15m310 ensemble. The different flow-time values are slightly shifted horizontally for visual clarity.

negative parity interpolating operator, constructed as in Refs. [144,145]. The fit Ansatz describing a $\bar{q}_1 q_2$-meson correlation functions is given by

$$C_{\text{2pt}}^{q_1q_2}(t) = \sum_n z_n^{q_1q_2} z_n^{q_1q_2\dagger}(e^{-E_n^{q_1q_2}t} + e^{-E_n^{q_1q_2}(T-t)}) + (-1)^t z^{\text{osc}} z^{\text{osc}\dagger}(e^{-E^{\text{osc}}t} + e^{-E^{\text{osc}}(T-t)}), \quad (6)$$

where we define z_n as the overlap factor of the nth state with energy E_n and the superscript osc. denotes the overlap and energy of the oscillating mode.

In order to determine the pseudoscalar decay constants, we utilize the five-dimensional (5D) Ward identity relating the renormalized decay constants to various correlation functions including those used to determine the values of m_{res} [146,147],

$$F^{q_1q_2} = z_p^{q_1q_2} \frac{m^{q_1} + m_{\text{res}}^{q_1} + m^{q_2} + m_{\text{res}}^{q_2}}{\sqrt[3]{E_0^{q_1q_2}}}, \quad (7)$$

where z_p denotes the point-sink overlap factor. This normalization is such that the physical pion decay constant is $F_\pi = 92.2$ MeV.

In order to determine the axial renormalization constants, we can also compute the bare values of $F^{q_1q_2}$ using the 4D axial-vector current,

$$C_{\text{axial}}^{q_1q_2} = \partial_4 \langle 0|A_4(t)P_S(0)|0\rangle = -\sum_n f_n^{q_1q_2} z_{s,n}^{q_1q_2}(e^{-E_n^{q_1q_2}t} + e^{-E_n^{q_1q_2}(T-t)}) - (-1)^t f^{\text{osc}} z_s^{\text{osc}}(e^{-E^{\text{osc}}t} + e^{-E^{\text{osc}}(T-t)}), \quad (8)$$

where $f_0^{q_1q_2} = \sqrt{E_0^{q_1q_2}} F^{q_1q_2}/Z_A$ with renormalization coefficient Z_A and z_s is the same ground-state overlap factor determined in the two-point function.

For the nucleon two-point correlation function, we use the fit Ansatz analogous to Eq. (6) without the oscillating state and wraparound terms.

B. Analysis strategy

The correlator analysis is performed using the PYTHON package LSQFIT [148]. We perform a chained fit [149] to the light and strange m_{res} correlator; the pion, kaon, and $\bar{s}s$-meson two-point and axial correlators; and the nucleon two-point correlator. In particular, as part of the chained fit, we perform a simultaneous fit to the pseudoscalar two-point (point- and smeared-sink) and axial correlators and to the nucleon point- and smeared-sink correlators. The chained fit implementation in LSQFIT preserves all correlations by numerically implementing the propagation of error under the assumption that all parameters are Gaussian distributed. We use the resulting correlated posterior distributions to propagate all subsequent uncertainties (e.g., ratios) without performing any bootstrap resampling.

For the pseudoscalar correlators, we truncate the fit Ansatz at $2 + 1$ states, where the $+1$ denotes the oscillating state. For the nucleon correlator, we perform a two-state fit. For the pseudoscalar correlators, in an independent analysis, using similar fit regions, we observe using three states without oscillating modes results in a consistent determination of the ground-state masses and overlap factors. Further, using an unconstrained, single-state fit in the late time region also results in consistent ground-state parameters.

We choose unconstraining ground-state priors such that the prior widths are at least an order of magnitude wider than the width of the posterior distribution. The oscillating-state energy splitting is chosen to be at the lattice cutoff scale. The first excited-state energy splitting is chosen to be at the two-pion threshold. Details on our prior choices are given in Table IX.

The fit region is chosen such that $t_{\text{min}} \sim 1$ fm and $t_{\text{max}} \sim 2.3$ fm for all pseudoscalar correlators. For the nucleon correlator analysis, $t_{\text{min}} \sim 0.6$ fm and $t_{\text{max}} \sim 1.4$ fm are chosen for all ensembles. It is necessary to fit the nucleon correlator closer to the origin due to the poorer signal-to-noise ratio when compared to the pseudoscalar observables. Explicit fit regions in lattice units are given in Table X. We

observe that all final correlator fits are in the region of stability for varying $t_{\min}$ and $t_{\max}$, including the more aggressive nucleon analysis, indicating that the results are free of excited-state contamination.

C. Observations about flow-time dependence

From our calculations, there are a few substantial benefits one observes from the use of the gradient-flow smearing. Before discussing these, we first comment on the strong oscillations observed at small flow time in the pseudoscalar correlators. In Fig. 1, we observe a strong signal for an oscillating excited state with $(-1)^t$ behavior (where t is the Euclidean time) at small flow times, most notably for $t_{gf} = 0.2$. These oscillating modes become completely damped out for $t_{gf} \geq 0.6$, with the statistics used in this work.

The first significant benefit observed is that as the flow time is increased a dramatic reduction of the chiral symmetry breaking properties of the valence MDWF action is achieved. This can be observed in the significant reduction in m_{res} at fixed pion mass or, similarly, the values of Z_A approaching 1 for all gauge couplings, both of which are depicted in Fig. 2. With the tuning we have chosen, to hold the pion mass, as well as L_5, M_5, b_5, and c_5, fixed as we vary the flow time, we observe an exponential reduction in m_{res} as the flow time is increased. Though not depicted in these figures or tables, we also studied the dependence of m_{res} on L_5 as the flow time was varied. We find that for small flow time, the reduction in m_{res} as L_5 increases is power law, indicating the 5D zero-mode contributions are dominating the residual chiral symmetry breaking. As we increase the flow time, m_{res} begins to fall off exponentially in L_5, indicating the gradient-flow smearing suppresses these zero-mode contributions.

Another significant benefit we observe is that stochastic fluctuations become smaller for increasing flow time because the gradient flow smearing procedure suppresses the ultraviolet noise. This is observed from the sample effective mass plots of the nucleon and pion in Fig. 1. The gradient flow is applied in all four spacetime directions, so the neighboring time slices become more correlated, rendering a direct comparison of the effective mass plots more complicated. However, the list of fitted quantities in Table VIII demonstrates the correlated stochastic uncertainties are reduced for increasing flow time. Comparing the $t_{gf} = 1$ to $t_{gf} = 0.2$ results, we observe approximately a factor of $\sqrt{2}$ reduction of the stochastic uncertainty for equal computing cost for all quantities other than the pseudoscalar meson masses.

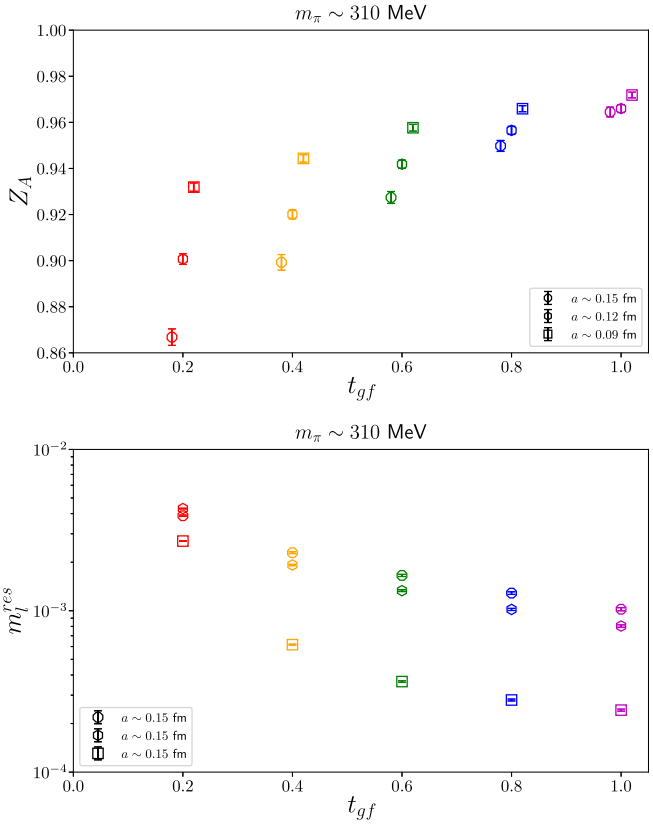

FIG. 2. Z_A (top) and m_l^{res} (bottom) as a function of flow time on the $m_\pi \simeq 310$ MeV ensembles. The results of Z_A are slightly shifted horizontally for visual clarity.

V. FLOW TIME INDEPENDENCE OF CONTINUUM LIMIT

In Fig. 3, we show a continuum study of m_N/F_π and F_K/F_π on the $m_\pi \sim 310$ MeV ensembles, for all flow times used. We explore four different continuum extrapolation Ansätze for a quantity f:

$$f(a/w_0) = \begin{cases} f_0, & \text{constant}, \\ f_0 + f_2 \frac{a^2}{w_0^2}, & \text{linear in } a^2, \\ f_0 + \alpha_s f'_2 \frac{a^2}{w_0^2}, & \text{linear in } \alpha_s a^2, \\ f_0 + f_4 \frac{a^4}{w_0^4}, & \text{quadratic in } a^2. \end{cases} \tag{9}$$

The gradient flow scale w_0 was first defined in Ref. [150], and a value of $w_0[150] = 0.1755(18)(04)$ fm was determined. The value determined in Ref. [151] is similar with a slight discrepancy, $w_0[151] = 0.1714(^{15}_{12})$ fm. We use this value as we are using the same ensembles on which it was determined. With only three lattice spacings, we choose not to perform an extrapolation in both a^2 and either $\alpha_s a^2$ or a^4 simultaneously. However, we observe the value of f_2 for both m_N/F_π and F_K/F_π to be small and often consistent with zero. This motivates exploring the linear in $\alpha_s a^2$ and a^4 fits as estimates of systematic uncertainties in the continuum extrapolation. We find all four continuum extrapolations show consistency at the 1-sigma level, both between all four different fit Ansätze and also between the

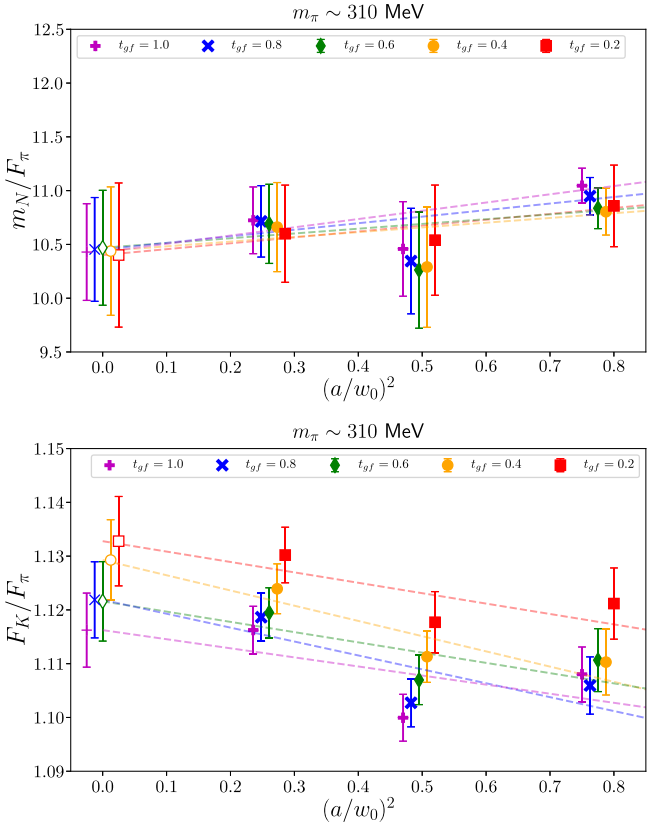

FIG. 3. Flow time (in)dependence of m_N/F_π and F_K/F_π on the $m_\pi \sim 310$ MeV ensembles. The filled in symbols are the results of our calculations, and the open symbols clustered at $a/w_0 = 0$ are the continuum extrapolated results using the simple Ansatz of a constant plus an $(a/w_0)^2$ term. The results are slightly shifted horizontally for visual clarity.

various flow-time extrapolations. In Fig. 3, we display the continuum extrapolation using the Ansatz linear in $(a/w_0)^2$. The quark-mass-independent values of a/w_0 and α_s are taken from Ref. [151].

For m_N/F_π, we observe minimal discretization corrections with a very small slope in $(a/w_0)^2$. For F_K/F_π, a quantity which is determined much more precisely for equal stochastic sampling, we observe mild, though still quite small, discretization corrections. While the discretization corrections are basically flow-time independent for m_N/F_π, they seem to become more pronounced for F_K/F_π as the flow time is increased. There is an indication of the presence of higher order quartic in a/w_0 corrections, but we are not able to resolve these with the numerical results in this work. Previous studies of the heavy-light decay constants observed that large amounts of APE smearing [152] could induce significant higher order discretization effects [153]. It is possible that the larger t_{gf} smearings are having a similar effect on the strange quark, and thus the value of F_K, at the subpercent level. These potential systematic uncertainties should be explored in more detail for a subpercent calculation of F_K/F_π using this action.

A. Mixed-meson mass corrections

In order to use the MA EFT extrapolation formulas, there are a few additional quantities which must be determined from the MALQCD calculations. At NLO in the MA EFT expansion, one needs to know the masses of the mixed valence-sea mesons which propagate in virtual loops and the value of the partial quenching parameter which controls the unitarity violating contributions [65,68]. In a general MALQCD calculation with a chirally symmetric valence action, one has

$$\begin{aligned} m_{vs}^2 &= \frac{1}{2}(m_{vv}^2 + m_{ss}^2) + a^2\tilde{\Delta}_{\text{Mix}}, \\ \Delta_{\text{PQ}}^2 &= m_{ss}^2 - m_{vv}^2, \end{aligned} \tag{10}$$

where m_{vv} is the mass of the pseudoscalar valence-valence meson, m_{ss} is the mass of the pseudoscalar sea-sea meson including possible additive discretization corrections, and $a^2\tilde{\Delta}_{\text{Mix}}$ is an additional additive discretization correction to the mass of a meson composed of one valence and one sea quark. For our MALQCD calculations, these two quantities are given by [65,68,69]

$$\begin{aligned} m_{vs}^2 &= \frac{1}{2}(m_{vv}^2 + m_{ss,5}^2) + a^2\tilde{\Delta}_{\text{Mix}}, \\ a^2\tilde{\Delta}_{\text{Mix}} &= a^2\Delta_{\text{Mix}} + \frac{a^2}{8}\Delta_A + \frac{3a^2}{16}\Delta_T + \frac{a^2}{8}\Delta_V + \frac{a^2}{32}\Delta_I, \\ a^2\Delta_{\text{Mix}} &= \frac{8a^2 C_{\text{Mix}}}{F^2}, \\ \Delta_{\text{PQ}}^2 &= m_{ss,5}^2 + a^2\Delta_I - m_{vv}^2, \end{aligned} \tag{11}$$

where $m_{ss,5}$ is the mass of the taste-5 pseudoscalar meson, $a^2\Delta_B$ are the taste splittings between the other taste-meson and the taste-5 meson, $a^2\Delta_B = m_B^2 - m_5^2$, F is the leading order pion decay constant, and C_{Mix} is the LEC of a new operator present in the MA EFT Lagrangian at $\mathcal{O}(a^2)$. The mixed-meson mass splitting, $a^2\Delta_{\text{Mix}}$, is universal at leading order in the MA EFT expansion [62], regardless of the taste of the staggered sea-quark partnered with the DW quark. In Ref. [66], it was observed that there is a noticeable quark-mass dependence of the mixed-meson splitting, as defined, e.g., for the pion

$$\Delta m_{vs}^2 \equiv m_{\pi,vs}^2 - \frac{1}{2}(m_{\pi,DW}^2 + m_{\pi,5}^2). \tag{12}$$

There are three common methods of incorporating these discretization corrections:

(i) Power-series expand the discretization corrections about $a = 0$, and use a continuum EFT extrapolation enhanced by general corrections of the form a^2, $a^2\alpha_S$, etc.

(ii) Extrapolate these mixed-meson discretization corrections to the chiral limit, and use a uniform correction for all mixed mesons with the full MA EFT expressions.

TABLE III. The mixed-meson mass spectrum determined on ensembles used in this work, with flow time $t_{gf} = 1$.

Ensemble	am_{uj}	am_{sj}	am_{ur}	am_{sr}
a15m310	0.300(6)	0.432(4)	0.444(5)	0.549(2)
a12m310	0.216(2)	0.334(2)	0.339(2)	0.430(1)
a09m310	0.150(1)	0.243(1)	0.247(1)	0.315(1)
a15m220	0.255(3)	0.416(3)	0.430(3)	0.543(1)
a12m220	0.178(2)	0.321(2)	0.335(2)	0.428(1)

(iii) Use the on-shell renormalized mixed-meson masses as they are on each ensemble with the full MA EFT expressions.

Provided the discretization corrections are under control, all three methods should agree in the continuum limit. It is useful, therefore, to determine the mixed-meson masses for all combinations of valence and sea quarks used in the MALQCD calculations.

In order to compute the mixed-meson spectrum, we need to construct pseudoscalar mesons composed of one MDWF and one HISQ fermion propagator. To compute the MDWF propagators, we have used the QUDA library interfaced from CHROMA with solutions generated with gauge-covariant Gaussian smeared sources [154]. To compute the HISQ propagators, we utilized the MILC code. To minimize the gauge noise, we similarly used a gauge-covariant source for the staggered fermions. This source was created in CHROMA, with routines added to the DEVEL branch to support writing a source file readable as a VECTOR_FIELD source by the MILC code. The MDWF fermions were converted to the DD_PAIRS format to be read by MILC, which was used to compute the mixed-meson and HISQ-HISQ pseudoscalar spectrum. To further reduce the gauge noise, the mixed-meson correlation functions were constructed with interpolating operators

$$\mathcal{O}_{vs} = \bar{q}_{\mathrm{val}}\gamma_5 q_{\mathrm{sea}} \tag{13}$$

as well as their Hermitian conjugates. The real parts of the averaged conjugate pairs of correlation functions were then used to determine the spectrum. Correlation functions were computed with all possible pairings of light and strange quarks with one MDWF- and one HISQ-type quark propagator.

In Table III, we list the masses of mixed mesons computed in this work, using only flow time $t_{gf} = 1$ ensembles. In Table IV, we list the values of the splittings Δm_{vs}^2, defined as in Eq. (12), and m_{vv} and m_{ss} are the pseudoscalar masses of the valence-valence and sea-sea mesons, respectively. The values are listed in w_0 units where the quark-mass-independent values w_0/a are taken from Ref. [151]. We use the notation of Ref. [73] and denote the various mixed mesons as

$$\begin{aligned}
\phi_{uj} &= \text{pion: val light} = u, \text{ sea light} = j,\\
\phi_{ur} &= \text{kaon: val light} = u, \text{ sea strange} = r,\\
\phi_{sj} &= \text{kaon: val strange} = s, \text{ sea light} = j,\\
\phi_{sr} &= \bar{s}\gamma_5 s\text{: val strange} = s, \text{ sea strange} = r.
\end{aligned} \tag{14}$$

TABLE IV. The mixed-meson mass splittings [Eq. (12)] determined on ensembles used in this work, with flow time $t_{gf} = 1$. The values of w_0/a are determined from Ref. [151].

Ensemble	$w_0^2\Delta m_{uj}^2$	$w_0^2\Delta m_{sj}^2$	$w_0^2\Delta m_{ur}^2$	$w_0^2\Delta m_{sr}^2$
a15m310	0.0439(41)	0.0298(40)	0.0440(59)	0.0422(28)
a12m310	0.0214(17)	0.0123(29)	0.0199(30)	0.0206(22)
a09m310	0.0102(09)	0.0038(18)	0.0102(19)	0.0085(14)
a15m220	0.0488(38)	0.0341(58)	0.0488(60)	0.0410(36)
a12m220	0.0279(13)	0.0142(20)	0.0334(30)	0.0212(20)

VI. BENCHMARK CALCULATION OF $F_{K^\pm}/F_{\pi^\pm}$

After demonstrating the flow-time independence of m_N/F_π and F_K/F_π in the continuum limit and observing the advantages of larger smearing flow times t_{gf}, we provide a benchmark computation with all systematic errors estimated. In particular, we assess the effects of the extrapolation to the physical pion mass as well as to the continuum and infinite volume limit of F_K/F_π. At NLO in the three-flavors chiral expansion, this quantity depends upon only a single LEC, L_5 [155]. Therefore, with the limited number of ensembles used in this work, we can perform a full extrapolation to the physical point. Further, F_K/F_π is obtained with great precision from many different LQCD calculations, and it is one of the quantities reviewed in depth by the FLAG Working Group [8]. A comparison serves as an important benchmark calculation of our lattice action.

A. χPT extrapolation at different gradient flow times

We have three lattice spacings and two pion masses with different values of $m_\pi L$. Following our findings for the continuum extrapolation at $m_\pi \sim 310$ MeV, our chiral-continuum extrapolation is performed with the form

$$\begin{aligned}
\frac{F_K}{F_\pi} = 1 &+ \frac{5}{8}\frac{m_\pi^2}{\Lambda_\chi^2}\ell_\pi - \frac{1}{4}\frac{m_K^2}{\Lambda_\chi^2}\ell_K - \frac{3}{8}\frac{m_\eta^2}{\Lambda_\chi^2}\ell_\eta\\
&+ \frac{4(m_K^2 - m_\pi^2)}{\Lambda_\chi^2}(4\pi)^2\left[L_5(\Lambda_\chi) + \frac{a^2}{w_0^2}L_a\right].
\end{aligned} \tag{15}$$

In this expression, we have used the relation valid at NLO in the $SU(3)$ chiral expansion, $m_\eta^2 = 4m_K^2/3 - m_\pi^2/3$, and the definitions $\ell_\phi = \ln(m_\phi^2/\Lambda_\chi^2)$ ($\phi \in \{\pi, K, \eta\}$) and $\Lambda_\chi^2 = (4\pi)^2 F_K F_\pi$. We have also included the finite volume corrections from the radiative pion loops predicted at one loop in χPT [156,157], but we find they have an irrelevant effect on the fit with the precision we have. The discretization corrections are flavor independent, and so they must vanish in the $SU(3)$ flavor limit where $F_K/F_\pi = 1$ exactly. Therefore, we parametrize the discretization correction through an unknown LEC that accompanies a term proportional to $(m_K^2 - m_\pi^2)(a/w_0)^2$.

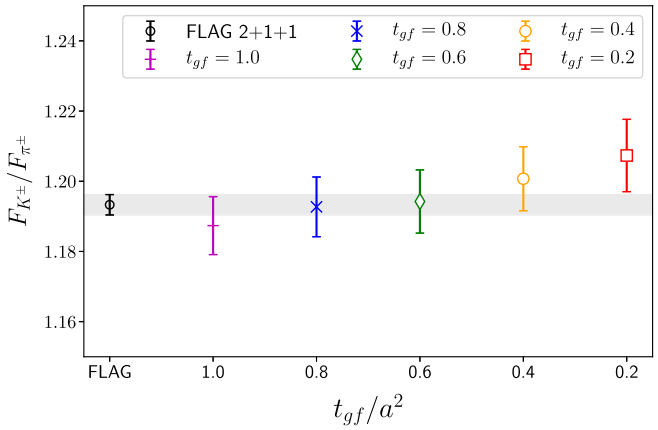

FIG. 4. Flow time (in)dependence of $F_{K^\pm}/F_{\pi^\pm}$ at the physical point $m_\pi \approx 135$ MeV in the continuum limit. The colored symbols are the results of our calculations extrapolated to the continuum limit and to the physical point using Eq. (15). The benchmark FLAG result is the leftmost black point, and it is consistent with our results at all flow times within 1-sigma (horizontal gray band). The linear trend in flow time observed is not present in the full continuum, chiral extrapolation analysis of different, but consistent, analysis of pseudoscalar correlation functions, so we believe this observed trend is not statistically significant.

Using the expression in Eq. (15), we fit the five ensembles used in this work for each flow-time independently. We then extrapolate these results to the isospin symmetric physical point, as determined by FLAG [8] with $m_\pi = 134.8(3)$ MeV and $m_K = 494.2(3)$ MeV. In order to compare with the FLAG determination, we must correct these results from the isospin symmetric point to the ratio of the charged decay constants, as prescribed in Eqs. (62) and (63) of the most recent FLAG review. In Fig. 4, we display our resulting values of $F_{K^\pm}/F_{\pi^\pm}$ for each flow time. We observe good quality in all our fits, as defined by the Q-value, which is the Bayesian analog to the p-value defined in Eq. (B4) of Ref. [158]. For comparison, we plot the FLAG determination of $F_{K^\pm}/F_{\pi^\pm}$ from the average of results using $N_f = 2+1+1$ ensembles. At the 1-sigma level, our results are self-consistent (flow-time independent) and also consistent with the FLAG average value. There is a trend of F_K/F_π with t_{gf} observed in Fig. 4. However, we do not believe this is statistically significant because the continuum, chiral analysis using different, but consistent, correlation function analysis results as input results in values of F_K/F_π which do not have a trend.

B. MA EFT extrapolation at $t_{gf} = 1$

While the numerical results are sufficient to constrain the unknown LECs, we note that for larger flow times the quality of the fit decreases, hinting at missing dependence upon the input parameters. For $t_{gf} = 1$, we have also computed the mixed-meson masses, and so we can perform the full MA EFT extrapolation. The NLO MA EFT expressions for $f_\pi = \sqrt{2}F_\pi$ and f_K are provided in Eqs. (C1) and (C2) of Ref. [65], respectively. In our case, we have tuned the valence quark masses such that the pion mass matches the taste-5 HISQ pion mass, which implies $\Delta_{ju} = \Delta_{rs} = 0$ in the reference expressions. Further, the mixed-meson mass splitting is independent of quark mass at LO, allowing us to simplify the extrapolation formula. To simplify transcribing the expression, we define

$$\begin{aligned}
\epsilon_\pi^2 &= \frac{m_\pi^2}{\Lambda_\chi^2}, \qquad \epsilon_{ju}^2 = \frac{m_\pi^2 + a^2\tilde{\Delta}_{\text{Mix}}}{\Lambda_\chi^2}, \\
\epsilon_K^2 &= \frac{m_K^2}{\Lambda_\chi^2}, \qquad \epsilon_{ru}^2 = \epsilon_{sj}^2 = \frac{m_K^2 + a^2\tilde{\Delta}_{\text{Mix}}}{\Lambda_\chi^2}, \\
\epsilon_{ss}^2 &= \frac{m_{ss}^2}{\Lambda_\chi^2}, \qquad \epsilon_{rs}^2 = \frac{m_{ss}^2 + a^2\tilde{\Delta}_{\text{Mix}}}{\Lambda_\chi^2}, \\
\delta_{PQ}^2 &= \frac{a^2\Delta_{\text{I}}}{\Lambda_\chi^2}, \qquad \epsilon_X^2 = \frac{4}{3}\epsilon_K^2 - \frac{1}{3}\epsilon_\pi^2 + \delta_{PQ}^2, \\
&\text{and} \quad \Lambda_\chi^2 = 16\pi^2 F_\pi F_K.
\end{aligned} \tag{16}$$

The resulting MA EFT expression is

$$\begin{aligned}
\frac{F_K}{F_\pi} = 1 &+ \frac{1}{2}\epsilon_{ju}^2\ell_{ju} + \frac{1}{8}\ell_\pi\left\{\epsilon_\pi^2 - \frac{\delta_{PQ}^2(\epsilon_X^2+\epsilon_\pi^2)}{\epsilon_X^2-\epsilon_\pi^2} + \frac{\delta_{PQ}^4\epsilon_X^2}{3(\epsilon_X^2-\epsilon_\pi^2)^2} - \frac{4\delta_{PQ}^4\epsilon_\pi^2}{3(\epsilon_X^2-\epsilon_\pi^2)(\epsilon_{ss}^2-\epsilon_\pi^2)}\right\} - \frac{1}{2}\epsilon_{sj}^2\ell_{sj} + \frac{1}{4}\epsilon_{ru}^2\ell_{ru} - \frac{1}{4}\epsilon_{rs}^2\ell_{rs} \\
&+ \frac{\ell_{ss}}{4}\left\{\epsilon_{ss}^2 + \frac{\delta_{PQ}^2(3\epsilon_{ss}^4 + 2(\epsilon_K^2-\epsilon_\pi^2)\epsilon_X^2 - 3\epsilon_{ss}^2\epsilon_X^2)}{3(\epsilon_X^2-\epsilon_{ss}^2)^2} - \frac{\delta_{PQ}^4(2\epsilon_{ss}^4 - \epsilon_X^2(\epsilon_{ss}^2+\epsilon_\pi^2))}{3(\epsilon_X^2-\epsilon_{ss}^2)^2(\epsilon_{ss}^2-\epsilon_\pi^2)}\right\} \\
&- \frac{3}{8}\epsilon_X^2\ell_X\left\{1 - \frac{2\delta_{PQ}^2/3}{(\epsilon_X^2-\epsilon_\pi^2)} + \frac{\delta_{PQ}^2[4(\epsilon_K^2-\epsilon_\pi^2)+6(\epsilon_{ss}^2-\epsilon_X^2)]}{9(\epsilon_X^2-\epsilon_{ss}^2)^2} + \frac{\delta_{PQ}^4/9}{(\epsilon_X^2-\epsilon_\pi^2)^2} - \frac{2\delta_{PQ}^4(2\epsilon_{ss}^2-\epsilon_\pi^2-\epsilon_X^2)}{9(\epsilon_X^2-\epsilon_{ss}^2)^2(\epsilon_X^2-\epsilon_\pi^2)}\right\} \\
&+ \frac{\delta_{PQ}^2(\epsilon_K^2-\epsilon_\pi^2)}{6(\epsilon_X^2-\epsilon_{ss}^2)} + \frac{\delta_{PQ}^4/24}{(\epsilon_X^2-\epsilon_\pi^2)} - \frac{\delta_{PQ}^4/12}{(\epsilon_X^2-\epsilon_{ss}^2)} - \frac{\delta_{PQ}^2}{8} + 4(\epsilon_K^2-\epsilon_\pi^2)(4\pi)^2 L_5(\Lambda_\chi).
\end{aligned} \tag{17}$$

In this expression, we have only included the NLO counterterm, which is the same as in $SU(3)\chi$PT, L_5. We observe that with this MA expression, the $a^2(m_K^2 - m_\pi^2)$ term is no longer needed to fit the data. When it is included, the fit returns a value of this

TABLE V. Physical extrapolation from the F_K/F_π analysis. The Q-value is the Bayesian analog of the p-value defined in Eq. (B4) of Ref. [158]. The logGBF denotes the log of the Gaussian Bayes factor and is used to select models under the Bayesian framework. The Bayes factors are suppressed for t_{gf} less than 1.0 since model comparisons are only sensible within the same data set.

t_{gf}	Function	$10^3 \times L_5$	F_K/F_π	Q-value	logGBF
0.2	Eq. (15)	5.55(1.17)	1.2102(105)	0.836	⋯
0.4	Eq. (15)	4.79(1.03)	1.2034(93)	0.808	⋯
0.6	Eq. (15)	4.05(1.02)	1.1968(92)	0.686	⋯
0.8	Eq. (15)	3.88(96)	1.1952(87)	0.448	⋯
1.0	Eq. (15)	3.27(93)	1.1898(84)	0.278	6.915
1.0	Eq. (17)	3.35(33)	1.1905(32)	0.296	11.947

LEC 2 orders of magnitude smaller than when using Eq. (15). For this analysis, we have taken the values of $w_0^2\Delta m_{ju}^2$ from Table IV, combined with the values of a/w_0 from Ref. [151] to determine the values of $a^2\tilde{\Delta}_{\mathrm{Mix}}$. We have used the values of $r_1^2a^2\Delta_{\mathrm{I}}$ and r_1/a from Ref. [112] to convert them to lattice units and combine them to form the necessary quantities in Eq. (16). We observe that the MA expression is approximately 150 times more likely to reproduce the observed data when compared to $SU(3)$ χPT, as determined by the Bayes factors given in Table V, providing very strong evidence that the MA expression provides the more correct physical point extrapolation. We leave further investigation of F_K/F_π with more statistics and more ensembles to future work.

VII. MDWF IN QUDA: OPTIMIZATIONS AND PERFORMANCE

In order to efficiently perform the MDWF solves, we utilize the GPU implementation of the MDWF operator and solver [159] from the highly optimized QUDA library [160,161]. We added the application programming interface (API) for accessing this solver to the CHROMA [122] package, which is publicly available in the most recent version.

The MDWF calculations were performed on three different GPU-enabled machines, Surface and RZHasGPU at Lawrence Livermore National Laboratory (LLNL) and Titan at Oak Ridge Leadership Computing Facility (OLCF).[1] The Surface cluster is composed of dual NVIDIA Tesla K40 cards with Intel Xeon E5-2670 CPU nodes. The RZHasGPU cluster is composed of dual NVIDIA Tesla K80 cards with Intel Xeon E5-2667 v3 CPU nodes. The Titan supercomputer is composed of single NVIDIA Tesla K20X cards with Advanced Micro Devices (AMD) Opteron CPU nodes. An interesting feature of the Titan nodes is the use of two eight-core NUMA nodes per node. We have found that we can provide two Message Passing Interface (MPI) ranks per GPU, by using both non-uniform memory access (NUMA) nodes, and achieve an approximately 69% performance boost with otherwise identical parameters. In Table VI, we list the sustained performance on the three machines achieved with the present implementation of the double-half mixed-precision MDWF solver. The single node performance is notable, and we are at present working on improving the strong scaling of the MDWF solver in QUDA through better overlapping of communication and computation. Additionally, a significant reduction of the condition number for the symmetric implementation of the MDWF operator has been observed [162]. QUDA supports both the symmetric and asymmetric implementations of the MDWF operator. Currently, CHROMA only supports the asymmetric operator, but we plan to investigate possible reduction in the time to solution from switching to the symmetric implementation.

TABLE VI. Performance of the double-half mixed precision MDWF solver in QUDA on the various compute nodes used with 2, 4 and 1 GPU per node on the Surface, RZHasGPU and Titan computers. The % of peak performance is obtained by comparing our sustained to the theoretical single-node single-precision performance. On Titan, we oversubscribe the GPUs by using 1 MPI rank per NUMA node, which amounts to 2 MPI ranks per GPU, resulting in a ∼69% performance boost.

Computer	GPUs	MPI ranks	Geometry	Performance [GFlops] Total	per node	% of peak
Surface	2	2	1 1 1 2	1250	1250	44%
RZHasGPU	4	4	1 1 1 4	1785	1785	48%
Titan	8	16	1 1 2 8	2885	0361	25%
Titan	16	32	1 2 2 8	4720	0295	20%
Titan	32	64	1 2 4 8	8500	0266	18%

VIII. CONCLUSIONS

In this work, we have motivated a new mixed lattice QCD action: Möbius domain-wall valence fermions solved with the dynamical $N_f = 2 + 1 + 1$ HISQ sea fermions after a gradient smearing algorithm is used to filter out UV modes of the gluons. To retain the correct continuum limit, the gradient flow time is held fixed in lattice units, such that any dependence upon this new scale also vanishes in the continuum limit. We demonstrate the flow-time independence of the continuum limit by computing two sample quantities, F_K/F_π and m_N/F_π. An extrapolation of F_K/F_π to the continuum, infinite volume, and physical pion and kaon mass point is consistent with the FLAG average of the $N_f = 2 + 1 + 1$ LQCD results for all flow times explored in this work.

For flow time of $t_{gf} = 1$, we estimate the total systematic error from different chiral and continuum fits to be smaller than our current statistical uncertainty. Of particular note, we also demonstrate that the gradient flow smearing highly suppresses sources of residual chiral symmetry breaking in the action for moderate values of the flow time: the axial

[1]Some of the early tuning and flow-time dependence studies were performed at the JLab High Performance Computing Center and at the Fermilab Lattice Gauge Theory Computational Facility.

renormalization constant becomes effectively lattice spacing independent and close to 1 for all ensembles at a flow time of $t_{gf} = 1$; the residual chiral symmetry breaking, measured by the quantity m_{res}, is exponentially damped with increasing flow time and less than 10% of the input light quark mass for all ensembles, including the physical quark-mass ensembles, with $t_{gf} = 1$ and moderate values of L_5.

This action, coupled with the use of the highly optimized QUDA library, provides an economical method of performing LQCD calculations with an action that respects chiral symmetry to a high degree. The MILC Collaboration has a long history of making their configurations freely available to all interested parties. The breadth of parameters used in the generation of the HISQ ensembles allows users to fully control all LQCD systematics: notably the continuum, and infinite volume extrapolations, as well as a physical quark-mass interpolation.

We have plans to use this action for computing various quantities relevant to fundamental nuclear and high-energy physics research, detailed, for example, in the Nuclear Science Advisory Committee (NSAC) Long Range Plan for Nuclear Science and the High Energy Physics Advisory Panel (HEPAP) P5 Strategic Plan for U.S. Particle Physics. So far, we have used this mixed action to demonstrate the benefits of a new method for computing hadronic matrix elements [142], applied this method to a precise determination of g_A [143], and we have computed the $\pi^- \to \pi^+$ transition matrix elements relevant for the scenario in which heavy lepton-number violating physics beyond the Standard Model contributes to the hypothesized neutrinoless double beta decay of large nuclei [141].

ACKNOWLEDGMENTS

We gratefully acknowledge the MILC Collaboration for use of the dynamical HISQ ensembles [111,112]. The two new ensembles we generated can be made available to any interested person or group. We thank Carleton DeTar and Doug Toussaint for help compiling and using the MILC code at LLNL and understanding how to write source fields from CHROMA that can be read by MILC for the construction of the mixed-meson correlation functions. We also thank Claude Bernard for useful correspondence regarding scale setting and taste violations with the HISQ action. Part of this work was performed at the Kavli Institute for Theoretical Physics supported by National Science Foundation (NSF) Grant No. PHY-1125915. The software used for this work was built on top of the CHROMA software suite [122] and the highly optimized QCD GPU library QUDA [160,161]. We also utilized the highly efficient HDF5 I/O Library [163] with an interface to HDF5 in the USQCD QDP++ package that was added with SciDAC 3 support (CalLat) [164], as well as the MILC software for solving for HISQ propagators. Finally, the high performance computing (HPC) jobs were efficiently managed with a BASH job manager, METAQ [165], capable of intelligently backfilling idle nodes in sets of nodes bundled into larger jobs submitted to HPC systems. METAQ was developed with SciDAC 3 support (CalLat) and is available on GITHUB. The numerical calculations in this work were performed at the Jefferson Lab High Performance Computing Center and the Fermilab Lattice Gauge Theory Computational Facility on facilities of the USQCD Collaboration, which are funded by the Office of Science of the U.S. Department of Energy; Lawrence Livermore National Laboratory on the Surface and RZhasGPU GPU clusters as well as the Cab CPU and Vulcan BG/Q clusters; and the Oak Ridge Leadership Computing Facility at the Oak Ridge National Laboratory, which is supported by the Office of Science of the U.S. Department of Energy under Contract No. DE-AC05-00OR22725, on the Titan machine through a DOE Innovative and Novel Computational Impact on Theory and Experiment (INCITE) award (CalLat). We thank the Lawrence Livermore National Laboratory Institutional Computing Grand Challenge program for the computing allocation. This work was performed with support from Laboratory Directed Research and Development (LDRD) funding from LLNL 13-ERD-023 (E. B., E. R., and P. V.) and by the RIKEN Special Postdoctoral Researcher program (E. R.). This work is supported in part by the DFG and the NSFC through funds provided to the Sino-German CRC 110 "Symmetries and the Emergence of Structure in QCD" (E. B.). This work was also performed under the auspices of the U.S. Department of Energy by Lawrence Livermore National Laboratory under Contract No. DE-AC52-07NA27344 (E. B., E. R., and P. V.); under which Jefferson Science Associates, Limited Liability Corporation (LLC), manages and operates Jefferson Lab (B. J. and K. O.) which includes funding from the DOE Office Of Science, Offices of Nuclear Physics, High Energy Physics and Advanced Scientific Computing Research under the SciDAC program (USQCD) (B. J.); under Contract No. DE-AC02-05CH11231, through which the Regents of the University of California manage and operate Lawrence Berkeley National Laboratory and the National Energy Research Scientific Computing Center (C. C. C., T. K., and A. W. L.). This work was further performed under the auspices of the U.S. Department of Energy, Office of Science, Office of Nuclear Physics, under Contracts No. DE-FG02-04ER41302 (C. M. B. and K. N. O.), No. DE-SC00046548 (A. N.), and No. DE-SC0015376, Double-Beta Decay Topical Collaboration (A. W. L.); by the Office of Advanced Scientific Computing Research, Scientific Discovery through Advanced Computing (SciDAC) program under Award No. KB0301052 (E. B., T. K., and A. W. L.); and by the DOE Early Career Research Program, Office of Nuclear Physics under FWP NQCDAWL (C. C. C. and A. W. L.).

APPENDIX A: TABLES OF FLOW-TIME DEPENDENCE

Here, we provide tables of the various quantities computed in this work on the different flow times used. Tuned quark masses and measured renormalization constants are reported in Table VII, while hadron masses and meson decay constants are summarized in Table VIII.

TABLE VII. The tuned values of the MDWF light and strange quark masses on various ensembles for various flow times. We also list the values of the average plaquette after applying the gradient flow as well as $m_{\rm res}$ and the renormalization constants.

Ensemble	M_5	L_5	b_5	c_5	t_{gf}	Plaquette	am_l^{mdwf}	$am_l^{\rm res}$	Z_A^{ll}	am_s^{mdwf}	$am_s^{\rm res}$	Z_A^{ls}
a15m310	1.3	12	1.5	0.5	0.2	0.87701(2)	0.00970	0.003882(38)	0.8668(36)	0.06810	0.003022(31)	0.8740(13)
					0.4	0.95521(1)	0.01160	0.002290(29)	0.8993(34)	0.07380	0.001668(22)	0.9074(12)
					0.6	0.97723(1)	0.01250	0.001656(26)	0.9274(26)	0.08000	0.001163(19)	0.9389(12)
					0.8	0.98560(1)	0.01480	0.001287(24)	0.9498(24)	0.08520	0.000880(17)	0.9608(11)
					1.0	0.98964(1)	0.01580	0.001022(23)	0.9645(21)	0.09020	0.000685(15)	0.9760(09)
a12m310	1.2	8	1.25	0.25	0.2	0.89320(1)	0.00680	0.004298(22)	0.9007(23)	0.05300	0.003416(18)	0.9034(10)
					0.4	0.96401(1)	0.00960	0.001922(18)	0.9201(20)	0.05830	0.001352(15)	0.9243(07)
					0.6	0.98251(1)	0.01086	0.001332(17)	0.9418(18)	0.06280	0.000860(13)	0.9464(07)
					0.8	0.98925(0)	0.01176	0.001019(15)	0.9565(18)	0.06650	0.000615(11)	0.9608(07)
					1.0	0.99242(0)	0.01260	0.000804(14)	0.9660(17)	0.06930	0.000467(09)	0.9705(06)
a09m310	1.1	6	1.25	0.25	0.2	0.91073(0)	0.00543	0.002704(07)	0.9319(18)	0.03880	0.002359(05)	0.9343(05)
					0.4	0.97236(0)	0.00798	0.000616(05)	0.9444(16)	0.04330	0.000459(04)	0.9452(06)
					0.6	0.98721(0)	0.00850	0.000364(04)	0.9577(15)	0.04500	0.000251(03)	0.9590(05)
					0.8	0.99239(0)	0.00921	0.000280(04)	0.9659(13)	0.04780	0.000189(02)	0.9679(04)
					1.0	0.99478(0)	0.00951	0.000242(04)	0.9719(13)	0.04910	0.000169(02)	0.9739(04)
a15m220	1.3	16	1.75	0.75	0.2	0.87718(1)	0.00425	0.002254(18)	0.8634(38)	0.06810	0.001699(17)	0.8713(12)
					0.4	0.95535(1)	0.00532	0.001356(16)	0.8892(33)	0.07380	0.000953(14)	0.9064(12)
					0.6	0.97735(1)	0.00615	0.000966(14)	0.9221(31)	0.08000	0.000658(11)	0.9398(13)
					0.8	0.98570(1)	0.00668	0.000733(11)	0.9456(27)	0.08520	0.000492(10)	0.9617(11)
					1.0	0.98973(1)	0.00712	0.000567(10)	0.9610(26)	0.09020	0.000374(09)	0.9765(09)
a12m220	1.2	12	1.5	0.5	0.2	0.89332(1)	0.00365	0.001562(11)	0.8923(25)	0.05480	0.001085(10)	0.9026(21)
					0.4	0.96410(0)	0.00456	0.000935(09)	0.9132(22)	0.05880	0.000582(07)	0.9240(17)
					0.6	0.98259(0)	0.00522	0.000673(08)	0.9409(37)	0.06280	0.000391(06)	0.9466(14)
					0.8	0.98931(0)	0.00575	0.000511(07)	0.9546(28)	0.06660	0.000286(05)	0.9621(12)
					1.0	0.99248(0)	0.00600	0.000390(05)	0.9615(22)	0.06930	0.000216(04)	0.9718(11)

TABLE VIII. Various hadronic quantities determined at different flow times. The posterior distributions related to meson and baryon correlation functions are extracted using a $2+1$-state fit Ansatz for mesons and *two* states for the nucleons, as described in Secs. IV A and IV B. The meson two-point correlation functions are fit simultaneously with the 4D axial-vector current, and then a chained fit [149] is used to propagate all remaining correlations. The entire fit strategy is implemented under the Bayesian framework with LSQFIT [148].

Ensemble	t_{gf}	am_π	am_K	am_{ss}	aF_π	aF_K	am_N	F_K/F_π	m_N/F_π
a15m310	0.2	0.2352(13)	0.4025(12)	0.51904(87)	0.07781(85)	0.08724(85)	0.845(28)	1.1212(66)	10.86(38)
	0.4	0.2327(13)	0.4014(12)	0.51710(89)	0.07720(69)	0.08572(64)	0.834(15)	1.1103(61)	10.80(22)
	0.6	0.2286(11)	0.4004(12)	0.51673(91)	0.07599(54)	0.08439(53)	0.823(13)	1.1107(58)	10.84(19)
	0.8	0.2363(11)	0.4028(12)	0.51673(92)	0.07543(53)	0.08343(49)	0.826(11)	1.1059(53)	10.95(17)
	1.0	0.2367(12)	0.4046(12)	0.51858(94)	0.07436(51)	0.08239(46)	0.821(10)	1.1080(51)	11.05(16)
a12m310	0.2	0.18876(60)	0.3233(07)	0.41835(61)	0.06385(65)	0.07137(63)	0.673(32)	1.1177(57)	10.54(51)
	0.4	0.18842(62)	0.3233(07)	0.41773(60)	0.06306(53)	0.07008(47)	0.649(35)	1.1113(48)	10.29(56)
	0.6	0.18837(64)	0.3232(07)	0.41754(59)	0.06243(48)	0.06911(40)	0.641(34)	1.1070(46)	10.26(54)
	0.8	0.18833(65)	0.3234(07)	0.41776(58)	0.06196(44)	0.06832(36)	0.641(30)	1.1027(45)	10.35(49)
	1.0	0.18911(65)	0.3232(07)	0.41721(58)	0.06142(41)	0.06755(34)	0.642(27)	1.0999(44)	10.46(44)
a09m310	0.2	0.13982(42)	0.2411(04)	0.31227(36)	0.04578(45)	0.05174(47)	0.485(20)	1.1302(52)	10.60(45)
	0.4	0.14017(39)	0.2423(04)	0.31392(36)	0.04590(36)	0.05159(35)	0.489(18)	1.1239(46)	10.66(41)
	0.6	0.13860(38)	0.2396(04)	0.31041(37)	0.04568(33)	0.05113(31)	0.488(16)	1.1195(46)	10.69(37)
	0.8	0.14026(38)	0.2416(04)	0.31280(37)	0.04550(31)	0.05090(29)	0.488(14)	1.1186(45)	10.71(33)
	1.0	0.13978(38)	0.2405(04)	0.31129(38)	0.04521(30)	0.05047(28)	0.485(13)	1.1163(44)	10.72(31)
a15m220	0.2	0.16707(94)	0.3838(09)	0.51227(74)	0.07616(82)	0.08794(70)	0.788(37)	1.1546(74)	10.35(49)
	0.4	0.16668(82)	0.3848(09)	0.51195(72)	0.07521(74)	0.08638(58)	0.794(34)	1.1485(74)	10.56(47)

(Table continued)

TABLE VIII. *(Continued)*

Ensemble	t_{gf}	am_π	am_K	am_{ss}	aF_π	aF_K	am_N	F_K/F_π	m_N/F_π
	0.6	0.16683(79)	0.3852(08)	0.51184(70)	0.07425(67)	0.08481(51)	0.787(18)	1.1422(72)	10.60(27)
	0.8	0.16647(76)	0.3853(09)	0.51195(70)	0.07343(63)	0.08338(45)	0.776(29)	1.1355(71)	10.57(41)
	1.0	0.16629(85)	0.3866(09)	0.51388(70)	0.07231(61)	0.08205(42)	0.766(28)	1.1348(72)	10.59(40)
a12m220	0.2	0.13305(58)	0.3080(12)	0.41732(56)	0.05732(63)	0.06618(84)	0.629(28)	1.154(12)	10.97(50)
	0.4	0.13370(54)	0.3086(11)	0.41636(72)	0.05773(53)	0.06610(76)	0.581(48)	1.145(12)	10.06(85)
	0.6	0.13354(96)	0.3088(10)	0.41583(55)	0.05784(51)	0.06582(63)	0.620(27)	1.138(10)	10.73(48)
	0.8	0.13491(75)	0.3103(07)	0.41690(53)	0.05778(47)	0.06572(38)	0.621(23)	1.1374(69)	10.74(41)
	1.0	0.13424(66)	0.3097(07)	0.41618(52)	0.05731(45)	0.06514(35)	0.619(19)	1.1367(69)	10.80(36)

APPENDIX B: PRIORS FOR CORRELATOR FITS

In Table IX, we summarize the Bayesian priors used in the analysis of the mesonic two-point functions, together with the ones for the nucleon correlator and m_{res}. Notice that the priors are chosen to be independent of the gradient flow time.

TABLE IX. Priors for correlator fits in lattice units. The priors are all Gaussian distributed and listed as mean (standard deviation). The oscillating and first excited-state energies are defined as splitting from the ground state, where $\Delta_i \equiv \ln(E_i - E_0)$. This leads to a log-normal distributed energy splitting, which is positive definite, and as a result enforces a strict hierarchy of states. The priors are chosen to be flow-time independent.

Ensemble	E_0^π	$z_{0,p}^\pi$	$z_{0,s}^\pi$	E_0^K	$z_{0,p}^K$	$z_{0,s}^K$	E_0^{ss}	$z_{0,p}^{ss}$	$z_{0,s}^{ss}$
a15m310	0.2360(236)	0.255(255)	0.025(25)	0.4050(405)	0.198(198)	0.0198(198)	0.520(52)	0.182(182)	0.0185(185)
a12m310	0.190(19)	0.19(19)	0.02(2)	0.3220(322)	0.148(148)	0.0159(159)	0.4180(418)	0.142(142)	0.0152(152)
a09m310	0.140(14)	0.122(122)	0.0047(47)	0.2420(242)	0.1(1)	0.0039(39)	0.3120(312)	0.1(1)	0.0037(37)
a15m220	0.1660(166)	0.325(325)	0.031(31)	0.3850(385)	0.2(2)	0.02(2)	0.5150(515)	0.18(18)	0.0184(184)
a12m220	0.1340(134)	0.224(224)	0.0115(115)	0.310(31)	0.15(15)	0.0079(79)	0.4150(415)	0.137(137)	0.0073(73)
Ensemble	$\Delta_{\text{osc.}}^\pi$	$z_{\text{osc.},p}^\pi$	$z_{\text{osc.},s}^\pi$	$\Delta_{\text{osc.}}^K$	$z_{\text{osc.},p}^K$	$z_{\text{osc.},s}^K$	$\Delta_{\text{osc.}}^{ss}$	$z_{\text{osc.},p}^{ss}$	$z_{\text{osc.},s}^{ss}$
a15m310	0(1.45)	0(0.255)	0(0.0125)	0(1.45)	0(0.198)	0(0.01)	0(1.45)	0(0.182)	0(0.009)
a12m310	0(1.67)	0(0.19)	0(0.01)	0(1.67)	0(0.148)	0(0.008)	0(1.67)	0(0.142)	0(0.008)
a09m310	0(1.96)	0(0.122)	0(0.00235)	0(1.96)	0(0.1)	0(0.0018)	0(1.96)	0(0.1)	0(0.0018)
a15m220	0(1.8)	0(0.325)	0(0.015)	0(1.8)	0(0.2)	0(0.01)	0(1.8)	0(0.18)	0(0.009)
a12m220	0(2)	0(0.224)	0(0.0057)	0(2)	0(0.15)	0(0.004)	0(2)	0(0.137)	0(0.004)
Ensemble	Δ_1^π	$z_{1,p}^\pi$	$z_{1,s}^\pi$	Δ_1^K	$z_{1,p}^K$	$z_{1,s}^K$	Δ_1^{ss}	$z_{1,p}^{ss}$	$z_{1,s}^{ss}$
a15m310	−0.75(70)	0(0.255)	0(0.0125)	−0.75(70)	0(0.198)	0(0.01)	−0.75(70)	0(0.182)	0(0.009)
a12m310	−0.97(70)	0(0.19)	0(0.01)	−0.97(70)	0(0.148)	0(0.008)	−0.97(70)	0(0.142)	0(0.008)
a09m310	−1.26(70)	0(0.122)	0(0.00235)	−1.26(70)	0(0.1)	0(0.0018)	−1.26(70)	0(0.1)	0(0.0018)
a15m220	−1.1(7)	0(0.325)	0(0.015)	−1.1(7)	0(0.2)	0(0.01)	−1.1(7)	0(0.18)	0(0.009)
a12m220	−1.3(7)	0(0.224)	0(0.0057)	−1.3(7)	0(0.15)	0(0.004)	−1.3(7)	0(0.137)	0(0.004)
Ensemble	f_0^π	$f_{\text{osc.}}^\pi$	f_1^π	f_0^K	$f_{\text{osc.}}^K$	f_1^K	f_0^{ss}	$f_{\text{osc.}}^{ss}$	f_1^{ss}
a15m310	0.0387(387)	0(0.0387)	0(0.0387)	0.054(54)	0(0.054)	0(0.054)	0.0648(648)	0(0.0648)	0(0.0648)
a12m310	0.028(20)	0(0.028)	0(0.028)	0.04(4)	0(0.04)	0(0.04)	0.0485(485)	0(0.0485)	0(0.0485)
a09m310	0.0175(175)	0(0.0175)	0(0.0175)	0.0256(256)	0(0.0256)	0(0.0256)	0.0318(318)	0(0.0318)	0(0.0318)
a15m220	0.0309(309)	0(0.0309)	0(0.0309)	0.0522(522)	0(0.0522)	0(0.0522)	0.0636(636)	0(0.0636)	0(0.0636)
a12m220	0.0221(221)	0(0.0221)	0(0.0221)	0.0375(375)	0(0.0375)	0(0.0375)	0.047(47)	0(0.047)	0(0.047)
Ensemble	E_0^N	$z_{0,p}^N$	$z_{0,s}^N$	Δ_1^N	$z_{1,p}^N$	$z_{1,s}^N$	m_{res}^l	m_{res}^s	
a15m310	0.820(82)	0.0112(55)	4.1(4.1)E-4	−0.75(70)	0(0.112)	0(0.0021)	0(1)	0(1)	
a12m310	0.670(67)	0.006(3)	2.6(2.6)E-4	−1.0(7)	0(0.06)	0(0.0013)	0(1)	0(1)	
a09m310	0.50(5)	0.0024(12)	2.2(2.2)E-5	−1.27(68)	0(0.024)	0(1.1)E-4	0(1)	0(1)	
a15m220	0.760(76)	0.011(5)	4.2(4.2)E-4	−1.1(7)	0(0.11)	0(0.0021)	0(1)	0(1)	
a12m220	0.610(61)	0.0054(27)	7.9(7.0)E-5	−1.3(7)	0(0.054)	0(4)E-4	0(1)	0(1)	

TABLE X. Fit range in lattice units. The fit region is chosen to be approximately the same in physical units for all pseudoscalar correlator fits, as well as among the nucleon correlator fits. The nucleon correlation functions are fit closer to the origin because of the poorer signal-to-noise ratio as compared to pseudoscalar observables.

a	$C^{q_1q_2}$ $t_{\min}$	$C^{q_1q_2}$ $t_{\max}$	C^{N} $t_{\min}$	C^{N} $t_{\max}$
0.15 fm	7	15	4	10
0.12 fm	8	19	5	12
0.09 fm	12	25	7	16

APPENDIX C: CORRELATOR ANALYSIS FIT REGIONS

A summary of the fit regions for the two-point function analysis is shown in Table X for the three different ensembles used in this work. q_1q_2 superscripts identify mesonic states (π, ss, and K.)

APPENDIX D: TOPOLOGICAL CHARGE EVOLUTION ON HISQ ENSEMBLES

In this Appendix, we provide additional details for the $N_f = 2 + 1 + 1$ HISQ ensembles at heavy pion masses ($m_\pi \approx 350$ and 400 MeV). The ensembles have a lattice spacing of $\approx$0.12 fm, and we expect the topological charge to fluctuate along the molecular dynamics trajectory and be Gaussian distributed. This behavior is plotted in Fig. 5 for both ensembles. Each of the new ensembles is obtained by combining configurations from eight independent streams (collected after each stream has thermalized), and they are plotted together in Fig. 5. We solve the gradient flow equations with the Symanzik action to smooth out the HISQ gauge fields, with a step size of $\epsilon = 0.03$ and up to $n = 166$ iterations. We use the symmetric Clover discretization of the bosonic topological charge density operator $G_{\mu\nu}\tilde{G}_{\mu\nu}$.

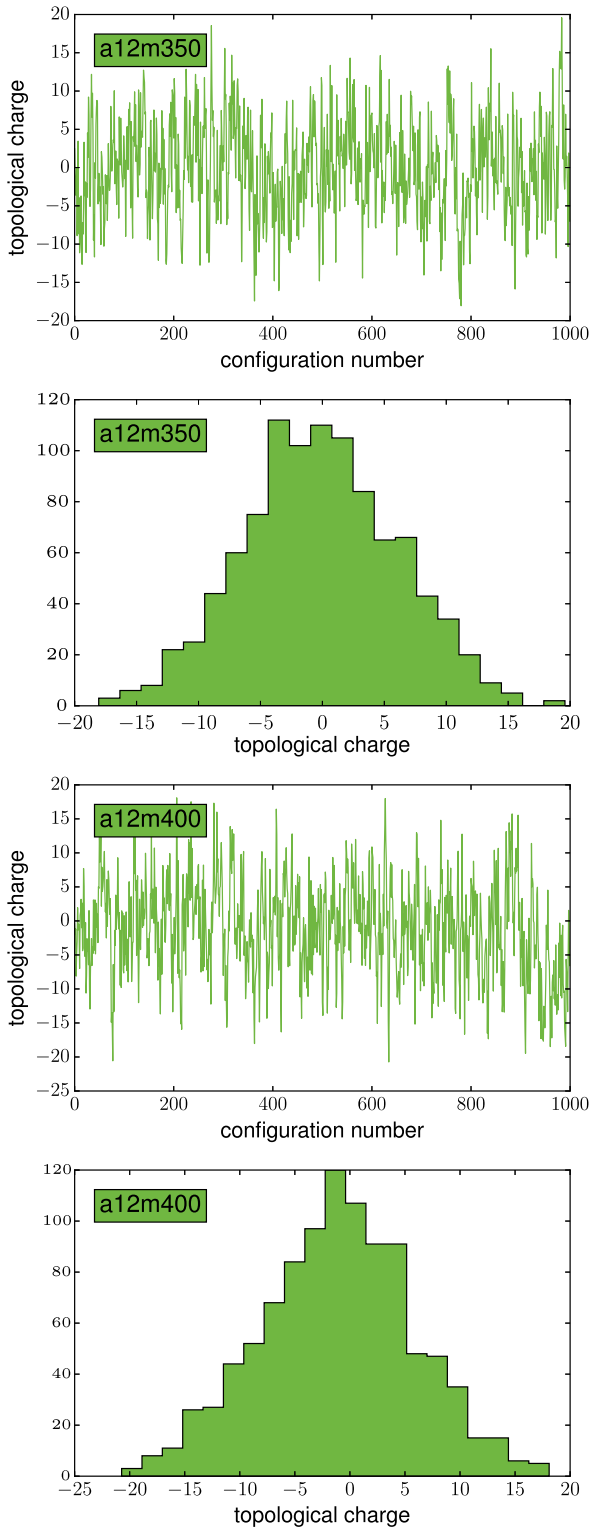

FIG. 5. Topological charge of the a12m350 and a12m400 ensembles at flow time $t_{gf} = 0.99$. The topological charge randomly fluctuates and shows no long correlation as a function of configuration number (Monte Carlo time) for both ensembles. The histograms show that the fluctuations are centered around zero, indicating the absence of CP violation, and are Gaussian distributed, indicating that the volumes are sufficiently large.

[1] H. Fritzsch and M. Gell-Mann, Current algebra: Quarks and what else?, *eConf* C720906V2, 135 (1972).

[2] H. Fritzsch, M. Gell-Mann, and H. Leutwyler, Advantages of the color octet gluon picture, Phys. Lett. **47B**, 365 (1973).

[3] D. J. Gross and F. Wilczek, Ultraviolet Behavior of Non-abelian Gauge Theories, Phys. Rev. Lett. **30**, 1343 (1973).

[4] H. David Politzer, Reliable Perturbative Results for Strong Interactions?, Phys. Rev. Lett. **30**, 1346 (1973).

[5] S. Weinberg,Phenomenological lagrangians, Physica Amsterdam **96A**, 327 (1979).

[6] K. Symanzik, Continuum limit and improved action in lattice theories. 1. Principles and φ^4theory, Nucl. Phys. **B226**, 187 (1983).

[7] K. Symanzik, Continuum limit and improved action in lattice theories. 2. O(N) nonlinear sigma model in perturbation theory, Nucl. Phys. **B226**, 205 (1983).

[8] S. Aoki *et al.*, Review of lattice results concerning low-energy particle physics, Eur. Phys. J. **C77**, 112 (2017).

[9] K. G. Wilson, Confinement of quarks, Phys. Rev. D **10**, 2445 (1974).

[10] B. Sheikholeslami and R. Wohlert, Improved continuum limit lattice action for QCD with Wilson fermions, Nucl. Phys. **B259**, 572 (1985).

[11] R. Frezzotti, P. Antonio Grassi, S. Sint, and P. Weisz (ALPHA Collaboration), Lattice QCD with a chirally twisted mass term, J. High Energy Phys. 08 (2001) 058.

[12] R. Frezzotti and G. C. Rossi, Chirally improving Wilson fermions. 1. O(a) improvement, J. High Energy Phys. 08 (2004) 007.

[13] J. B. Kogut and L. Susskind, Hamiltonian formulation of Wilson's lattice gauge theories, Phys. Rev. D **11**, 395 (1975).

[14] L. Susskind, Lattice fermions, Phys. Rev. D **16**, 3031 (1977).

[15] E. Marinari, G. Parisi, and C. Rebbi, Monte Carlo simulation of the massive Schwinger model, Nucl. Phys. **B190**, 734 (1981).

[16] C. Bernard, M. Golterman, Y. Shamir, and S. R. Sharpe, Comment on 'Chiral anomalies and rooted staggered fermions', Phys. Lett. B **649**, 235 (2007).

[17] C. Bernard, M. Golterman, and Y. Shamir, Observations on staggered fermions at non-zero lattice spacing, Phys. Rev. D **73**, 114511 (2006).

[18] M. Creutz, Chiral anomalies and rooted staggered fermions, Phys. Lett. B **649**, 230 (2007).

[19] C. Bernard, Order of the chiral and continuum limits in staggered chiral perturbation theory, Phys. Rev. D **71**, 094020 (2005).

[20] C. Bernard, Staggered chiral perturbation theory and the fourth-root trick, Phys. Rev. D **73**, 114503 (2006).

[21] Y. Shamir, Locality of the fourth root of the staggered-fermion determinant: Renormalization-group approach, Phys. Rev. D **71**, 034509 (2005).

[22] Y. Shamir, Renormalization-group analysis of the validity of staggered-fermion QCD with the fourth-root recipe, Phys. Rev. D **75**, 054503 (2007).

[23] C. Bernard, M. Golterman, and Y. Shamir, Effective field theories for QCD with rooted staggered fermions, Phys. Rev. D **77**, 074505 (2008).

[24] S. Durr and C. Hoelbling, Scaling tests with dynamical overlap and rooted staggered fermions, Phys. Rev. D **71**, 054501 (2005).

[25] S. Durr and C. Hoelbling, Lattice fermions with complex mass, Phys. Rev. D **74**, 014513 (2006).

[26] A. Hasenfratz and R. Hoffmann, Validity of the rooted staggered determinant in the continuum limit, Phys. Rev. D **74**, 014511 (2006).

[27] C. Bernard, M. Golterman, Y. Shamir, and S. R. Sharpe, 't Hooft vertices, partial quenching, and rooted staggered QCD, Phys. Rev. D **77**, 114504 (2008).

[28] S. R. Sharpe, Rooted staggered fermions: Good, bad or ugly?, *Proc. Sci.*, LAT2006 (2006) 022 [arXiv:hep-lat/0610094].

[29] A. S. Kronfeld, Lattice gauge theory with staggered fermions: How, where, and why (not), *Proc. Sci.*, LAT2007 (2007) 016 [arXiv:0711.0699].

[30] A. Bazavov *et al.* (MILC Collaboration), Nonperturbative QCD simulations with $2 + 1$ flavors of improved staggered quarks, Rev. Mod. Phys. **82**, 1349 (2010).

[31] H. Bech Nielsen and M. Ninomiya, Absence of neutrinos on a lattice. 1. Proof by homotopy theory, Nucl. Phys. **B185**, 20 (1981).

[32] H. Bech Nielsen and M. Ninomiya, Absence of neutrinos on a lattice. 2. Intuitive topological proof, Nucl. Phys. **B193**, 173 (1981).

[33] H. Bech Nielsen and M. Ninomiya, No go theorem for regularizing chiral fermions, Phys. Lett. **105B**, 219 (1981).

[34] P. H. Ginsparg and K. G. Wilson, A remnant of chiral symmetry on the lattice, Phys. Rev. D **25**, 2649 (1982).

[35] M. Lüscher, Exact chiral symmetry on the lattice and the Ginsparg-Wilson relation, Phys. Lett. B **428**, 342 (1998).

[36] D. B. Kaplan, A method for simulating chiral fermions on the lattice, Phys. Lett. B **288**, 342 (1992).

[37] Y. Shamir, Chiral fermions from lattice boundaries, Nucl. Phys. **B406**, 90 (1993).

[38] V. Furman and Y. Shamir, Axial symmetries in lattice QCD with Kaplan fermions, Nucl. Phys. **B439**, 54 (1995).

[39] R. Narayanan and H. Neuberger, Chiral determinant as an overlap of two vacua, Nucl. Phys. **B412**, 574 (1994).

[40] R. Narayanan and H. Neuberger, Chiral Fermions on the Lattice, Phys. Rev. Lett. **71**, 3251 (1993).

[41] R. Narayanan and H. Neuberger, A Construction of lattice chiral gauge theories, Nucl. Phys. **B443**, 305 (1995).

[42] A. Borici, Truncated overlap fermions, Nucl. Phys. B, Proc. Suppl. **83–84**, 771 (2000).

[43] A Borici, in *Lattice fermions and structure of the vacuum. Proceedings, NATO Advanced Research Workshop, Dubna, Russia, 1999* (Springer, Netherlands, 1999), p. 41.

[44] A. D. Kennedy, Algorithms for lattice QCD with dynamical fermions, Nucl. Phys. B, Proc. Suppl. **140**, 190 (2005).

[45] O. Bar, G. Rupak, and N. Shoresh, Simulations with different lattice Dirac operators for valence and sea quarks, Phys. Rev. D **67**, 114505 (2003).

[46] D. Bryant Renner, W. Schroers, R. Edwards, G. Tamminga Fleming, Ph. Hagler, J. W. Negele, K. Orginos, A. V. Pochinski, and D. Richards (LHPC Collaboration), Hadronic physics with domain-wall valence and improved staggered sea quarks, Nucl. Phys. B, Proc. Suppl. **140**, 255 (2005).

[47] K. Orginos and D. Toussaint (MILC Collaboration), Testing improved actions for dynamical Kogut-Susskind quarks, Phys. Rev. D **59**, 014501 (1998).
[48] K. Orginos, D. Toussaint, and R. L. Sugar (MILC Collaboration), Variants of fattening and flavor symmetry restoration, Phys. Rev. D **60**, 054503 (1999).
[49] C. W. Bernard, T. Burch, K. Orginos, D. Toussaint, T. A. DeGrand, C. E. Detar, S. Datta, S. A. Gottlieb, U. M. Heller, and R. Sugar, The QCD spectrum with three quark flavors, Phys. Rev. D **64**, 054506 (2001).
[50] R. G. Edwards, G. T. Fleming, Ph. Hagler, J. W. Negele, K. Orginos, A. V. Pochinsky, D. B. Renner, D. G. Richards, and W. Schroers (LHPC Collaboration), The Nucleon Axial Charge in Full Lattice QCD, Phys. Rev. Lett. **96**, 052001 (2006).
[51] Ph. Hagler *et al.* (LHPC Collaboration), Nucleon generalized parton distributions from full lattice QCD, Phys. Rev. D **77**, 094502 (2008).
[52] J. D. Bratt *et al.* (LHPC Collaboration), Nucleon structure from mixed action calculations using $2+1$ flavors of asqtad sea and domain wall valence fermions, Phys. Rev. D **82**, 094502 (2010).
[53] S. R. Beane, P. F. Bedaque, K. Orginos, and M. J. Savage (NPLQCD Collaboration), Nucleon-Nucleon Scattering from Fully-Dynamical Lattice QCD, Phys. Rev. Lett. **97**, 012001 (2006).
[54] S. R. Beane, T. C. Luu, K. Orginos, A. Parreño, M. J. Savage, A. Torok, and A. Walker-Loud (NPLQCD Collaboration), Precise determination of the $I=2$ pipi scattering length from mixed-action lattice QCD, Phys. Rev. D **77**, 014505 (2008).
[55] A. Walker-Loud *et al.*, Light hadron spectroscopy using domain wall valence quarks on an asqtad sea, Phys. Rev. D **79**, 054502 (2009).
[56] C. Aubin, J. Laiho, and R. S. Van de Water, The neutral kaon mixing parameter B(K) from unquenched mixed-action lattice QCD, Phys. Rev. D **81**, 014507 (2010).
[57] P. Langacker and H. Pagels, Chiral perturbation theory, Phys. Rev. D **8**, 4595 (1973).
[58] J. Gasser and H. Leutwyler, Chiral perturbation theory to one loop, Ann. Phys. (N.Y.) **158**, 142 (1984).
[59] H. Leutwyler, On the foundations of chiral perturbation theory, Ann. Phys. (N.Y.) **235**, 165 (1994).
[60] S. R. Sharpe and R. L. Singleton, Jr., Spontaneous flavor and parity breaking with Wilson fermions, Phys. Rev. D **58**, 074501 (1998).
[61] O. Bar, G. Rupak, and N. Shoresh, Chiral perturbation theory at $\mathcal{O}(a^2)$ for lattice QCD, Phys. Rev. D **70**, 034508 (2004).
[62] O. Bar, C. Bernard, G. Rupak, and N. Shoresh, Chiral perturbation theory for staggered sea quarks and Ginsparg-Wilson valence quarks, Phys. Rev. D **72**, 054502 (2005).
[63] B. C. Tiburzi, Baryons with Ginsparg-Wilson quarks in a staggered sea, Phys. Rev. D **72**, 094501 (2005); Erratum, Phys. Rev. D **79**, 039904(E) (2009.
[64] J.-W. Chen, D. O'Connell, R. S. Van de Water, and A. Walker-Loud, Ginsparg-Wilson pions scattering on a staggered sea, Phys. Rev. D **73**, 074510 (2006).
[65] J.-W. Chen, D. O'Connell, and A. Walker-Loud, Two meson systems with Ginsparg-Wilson valence quarks, Phys. Rev. D **75**, 054501 (2007).
[66] K. Orginos and A. Walker-Loud, Mixed meson masses with domain-wall valence and staggered sea fermions, Phys. Rev. D **77**, 094505 (2008).
[67] F.-J. Jiang, Mixed action lattice spacing effects on the nucleon axial charge, arXiv:hep-lat/0703012.
[68] J.-W. Chen, D. O'Connell, and A. Walker-Loud, Universality of mixed action extrapolation formulae, J. High Energy Phys. 04 (2009) 090.
[69] J.-W. Chen, M. Golterman, D. O'Connell, and A. Walker-Loud, Mixed action effective field theory: An addendum, Phys. Rev. D **79**, 117502 (2009).
[70] C. W. Bernard and M. F. L. Golterman, Partially quenched gauge theories and an application to staggered fermions, Phys. Rev. D **49**, 486 (1994).
[71] S. R. Sharpe and N. Shoresh, Physical results from unphysical simulations, Phys. Rev. D **62**, 094503 (2000).
[72] S. R. Sharpe and N. Shoresh, Partially quenched chiral perturbation theory without Φ_0, Phys. Rev. D **64**, 114510 (2001).
[73] J.-W. Chen and M. J. Savage, Baryons in partially quenched chiral perturbation theory, Phys. Rev. D **65**, 094001 (2002).
[74] S. R. Sharpe and R. S. Van de Water, Unphysical operators in partially quenched QCD, Phys. Rev. D **69**, 054027 (2004).
[75] D. Arndt and B. C. Tiburzi, Charge radii of the meson and baryon octets in quenched and partially quenched chiral perturbation theory, Phys. Rev. D **68**, 094501 (2003).
[76] A. Walker-Loud, Octet baryon masses in partially quenched chiral perturbation theory, Nucl. Phys. **A747**, 476 (2005).
[77] C. Bernard and M. Golterman, Transfer matrix for partially quenched QCD, *Proc. Sci.*, LATTICE2010 (2010) 252 [arXiv:1011.0184].
[78] C. Bernard and M. Golterman, On the foundations of partially quenched chiral perturbation theory, Phys. Rev. D **88**, 014004 (2013).
[79] S. R. Beane and M. J. Savage, Nucleons in two flavor partially quenched chiral perturbation theory, Nucl. Phys. **A709**, 319 (2002).
[80] S. R. Beane and M. J. Savage, Partially quenched nucleon-nucleon scattering, Phys. Rev. D **67**, 054502 (2003).
[81] D. Arndt and B. C. Tiburzi, Electromagnetic properties of the baryon decuplet in quenched and partially quenched chiral perturbation theory, Phys. Rev. D **68**, 114503 (2003); Erratum, Phys. Rev. D **69**, 059904(E) (2004).
[82] D. Arndt and B. C. Tiburzi, Baryon decuplet to octet electromagnetic transitions in quenched and partially quenched chiral perturbation theory, Phys. Rev. D **69**, 014501 (2004).
[83] B. C. Tiburzi and A. Walker-Loud, Decuplet baryon masses in partially quenched chiral perturbation theory, Nucl. Phys. **A748**, 513 (2005).
[84] B. C. Tiburzi, Baryon masses in partially quenched heavy hadron chiral perturbation theory, Phys. Rev. D **71**, 034501 (2005).

[85] B. C. Tiburzi and A. Walker-Loud, Strong isospin breaking in the nucleon and Delta masses, Nucl. Phys. **A764**, 274 (2006).

[86] D. O'Connell and M. J. Savage, Extrapolation formulas for neutron EDM calculations in lattice QCD, Phys. Lett. B **633**, 319 (2006).

[87] S. Prelovsek, Effects of staggered fermions and mixed actions on the scalar correlator, Phys. Rev. D **73**, 014506 (2006).

[88] C. Aubin, J. Laiho, and R. S. Van de Water, Discretization effects and the scalar meson correlator in mixed-action lattice simulations, Phys. Rev. D **77**, 114501 (2008).

[89] H. Na, C. M. Bouchard, G. Peter Lepage, C. Monahan, and J. Shigemitsu (HPQCD Collaboration), $B \to Dl\nu$ form factors at nonzero recoil and extraction of $|V_{cb}|$, Phys. Rev. D **92**, 054510 (2015); Erratum, Phys. Rev. D **93**, 119906(E) (2016).

[90] G. C. Donald, C. T. H. Davies, J. Koponen, and G. P. Lepage, Prediction of the D_s^* Width from a Calculation of its Radiative Decay in Full Lattice QCD, Phys. Rev. Lett. **112**, 212002 (2014).

[91] A. Li *et al.* (xQCD Collaboration), Overlap valence on $2+1$ flavor domain wall fermion configurations with deflation and low-mode substitution, Phys. Rev. D **82**, 114501 (2010).

[92] M. Lujan, A. Alexandru, Y. Chen, T. Draper, W. Freeman, M. Gong, F. X. Lee, A. Li, K. F. Liu, and N. Mathur, The Δ_{mix} parameter in the overlap on domain-wall mixed action, Phys. Rev. D **86**, 014501 (2012).

[93] M. Gong *et al.* (XQCD Collaboration), Strangeness and charmness content of the nucleon from overlap fermions on $2+1$-flavor domain-wall fermion configurations, Phys. Rev. D **88**, 014503 (2013).

[94] C. Allton *et al.* (RBC and UKQCD Collaborations), $2+1$ flavor domain wall QCD on a $(2\times fm)\times^3$lattice: Light meson spectroscopy with $L_s = 16$, Phys. Rev. D **76**, 014504 (2007).

[95] Y. Aoki *et al.* (RBC and UKQCD Collaborations), Continuum limit physics from $2+1$ flavor domain wall QCD, Phys. Rev. D **83**, 074508 (2011).

[96] S. Basak, S. Datta, M. Padmanath, P. Majumdar, and N. Mathur, Charm and strange hadron spectra from overlap fermions on HISQ gauge configurations, *Proc. Sci.*, LATTICE2012 (2012) 141 [arXiv:1211.6277].

[97] S. Basak, S. Datta, A. T. Lytle, M. Padmanath, P. Majumdar, and N. Mathur, Hadron spectra from overlap fermions on HISQ gauge configurations, *Proc. Sci.*, LATTICE2013 (2014) 243 [arXiv:1312.3050].

[98] S. Basak, S. Datta, N. Mathur, A. T. Lytle, P. Majumdar, and M. Padmanath (ILGTI Collaboration), Hadron spectra and Δ_{mix} from overlap quarks on a HISQ sea, *Proc. Sci.*, LATTICE2014 (2015) 083 [arXiv:1412.7248].

[99] N. Mathur, M. Padmanath, and R. Lewis, Charmed-bottom mesons from lattice QCD, *Proc. Sci.*, LATTICE2016 (2016) 100 [arXiv:1611.04085].

[100] T. Bhattacharya, S. D. Cohen, R. Gupta, A. Joseph, H.-W. Lin, and B. Yoon, Nucleon charges and electromagnetic form factors from $2+1+1$-flavor lattice QCD, Phys. Rev. D **89**, 094502 (2014).

[101] T. Bhattacharya, V. Cirigliano, S. Cohen, R. Gupta, A. Joseph, H.-W. Lin, and B. Yoon (PNDME Collaboration), Iso-vector and iso-scalar tensor charges of the nucleon from lattice QCD, Phys. Rev. D **92**, 094511 (2015).

[102] S. Durr *et al.*, Sigma term and strangeness content of octet baryons, Phys. Rev. D **85**, 014509 (2012); Erratum, Phys. Rev. D **93**, 039905(E) (2016).

[103] S. Durr *et al.*, Lattice Computation of the Nucleon Scalar Quark Contents at the Physical Point, Phys. Rev. Lett. **116**, 172001 (2016).

[104] Y.-B. Yang, A. Alexandru, T. Draper, J. Liang, and K.-F. Liu (xQCD Collaboration), πN and strangeness sigma terms at the physical point with chiral fermions, Phys. Rev. D **94**, 054503 (2016).

[105] R. Sabbir Sufian, Y.-B. Yang, A. Alexandru, T. Draper, J. Liang, and K.-F. Liu, Strange Quark Magnetic Moment of the Nucleon at the Physical Point, Phys. Rev. Lett. **118**, 042001 (2017).

[106] T. Bhattacharya, V. Cirigliano, S. Cohen, R. Gupta, H.-W. Lin, and B. Yoon, Axial, scalar and tensor charges of the nucleon from $2+1+1$-flavor lattice QCD, Phys. Rev. D **94**, 054508 (2016).

[107] Sz. Borsanyi *et al.* (Budapest-Marseille-Wuppertal Collaboration), Isospin Splittings in the Light Baryon Octet from Lattice QCD and QED, Phys. Rev. Lett. **111**, 252001 (2013).

[108] Sz. Borsanyi *et al.*, *Ab initio* calculation of the neutron-proton mass difference, Science **347**, 1452 (2015).

[109] D. A. Brantley, B. Joo, E. V. Mastropas, E. Mereghetti, H. Monge-Camacho, B. C. Tiburzi, and A. Walker-Loud, Strong isospin violation and chiral logarithms in the baryon spectrum, arXiv:1612.07733.

[110] E. Follana, Q. Mason, C. Davies, K. Hornbostel, G. P. Lepage, J. Shigemitsu, H. Trottier, and K. Wong (HPQCD and UKQCD Collaborations), Highly improved staggered quarks on the lattice, with applications to charm physics, Phys. Rev. D **75**, 054502 (2007).

[111] A. Bazavov *et al.* (MILC Collaboration), Scaling studies of QCD with the dynamical HISQ action, Phys. Rev. D **82**, 074501 (2010).

[112] A. Bazavov *et al.* (MILC Collaboration), Lattice QCD ensembles with four flavors of highly improved staggered quarks, Phys. Rev. D **87**, 054505 (2013).

[113] R. C. Brower, H. Neff, and K. Orginos, Mobius fermions: Improved domain wall chiral fermions, Nucl. Phys. B, Proc. Suppl. **140**, 686 (2005).

[114] R. C. Brower, H. Neff, and K. Orginos, M. fermions, Möbius fermions, Nucl. Phys. B, Proc. Suppl. **153**, 191 (2006).

[115] R. C. Brower, H. Neff, and K. Orginos, The möbius domain wall fermion algorithm, arXiv:1206.5214.

[116] H. Neuberger, Vector-like gauge theories with almost massless fermions on the lattice, Phys. Rev. D **57**, 5417 (1998).

[117] H. Neuberger, Exactly massless quarks on the lattice, Phys. Lett. B **417**, 141 (1998).

[118] P. M. Vranas, Chiral symmetry restoration in the Schwinger model with domain wall fermions, Phys. Rev. D **57**, 1415 (1998).

[119] Y. Kikukawa and T. Noguchi, Low-energy effective action of domain wall fermion and the Ginsparg-Wilson relation, Nucl. Phys. B, Proc. Suppl. **83–84**, 630 (2000).
[120] R. G. Edwards and U. M. Heller, Domain wall fermions with exact chiral symmetry, Phys. Rev. D **63**, 094505 (2001).
[121] A. D. Kennedy, Algorithms for dynamical fermions, arXiv: hep-lat/0607038.
[122] R. G. Edwards and B. Joo (SciDAC, Lattice Hadron Physics, and UKQCD Collaborations), The CHROMA software system for lattice QCD, Nucl. Phys. B, Proc. Suppl. **140**, 832 (2005).
[123] A. Hasenfratz and F. Knechtli, Flavor symmetry and the static potential with hypercubic blocking, Phys. Rev. D **64**, 034504 (2001).
[124] T. A. DeGrand, A. Hasenfratz, and T. G. Kovacs, Improving the chiral properties of lattice fermions, Phys. Rev. D **67**, 054501 (2003).
[125] T. A. DeGrand (MILC Collaboration), Kaon B parameter in quenched QCD, Phys. Rev. D **69**, 014504 (2004).
[126] S. Durr, C. Hoelbling, and U. Wenger, Staggered eigenvalue mimicry, Phys. Rev. D **70**, 094502 (2004).
[127] R. Narayanan and H. Neuberger, Infinite N phase transitions in continuum Wilson loop operators, J. High Energy Phys. 03 (2006) 064.
[128] M. Lüscher and P. Weisz, Perturbative analysis of the gradient flow in non-abelian gauge theories, J. High Energy Phys. 02 (2011) 051.
[129] M. Lüscher, Chiral symmetry and the Yang–Mills gradient flow, J. High Energy Phys. 04 (2013) 123.
[130] C. Morningstar and M. J. Peardon, Analytic smearing of SU(3) link variables in lattice QCD, Phys. Rev. D **69**, 054501 (2004).
[131] L. Del Debbio, A. Patella, and A. Rago, Space-time symmetries and the Yang-Mills gradient flow, J. High Energy Phys. 11 (2013) 212.
[132] H. Suzuki, Energy–momentum tensor from the Yang-Mills gradient flow, Prog. Theor. Exp. Phys. **2013**, 083B03 (2013).
[133] C. Monahan and K. Orginos, Finite volume renormalization scheme for fermionic operators, *Proc. Sci.*, Lattice2013 (2013) 443.
[134] M. Lüscher, Step scaling and the Yang-Mills gradient flow, J. High Energy Phys. 06 (2014) 105.
[135] T. Endo, K. Hieda, D. Miura, and H. Suzuki, Universal formula for the flavor non-singlet axial-vector current from the gradient flow, Prog. Theor. Exp. Phys. **2015**, 053B03 (2015).
[136] C. Monahan and K. Orginos, Locally smeared operator product expansions in scalar field theory, Phys. Rev. D **91**, 074513 (2015).
[137] C. Monahan and K. Orginos, Quasi parton distributions and the gradient flow, J. High Energy Phys. 03 (2017) 116.
[138] M. Lüscher, Properties and uses of the Wilson flow in lattice QCD, J. High Energy Phys. 08 (2010) 071.
[139] R. Lohmayer and H. Neuberger, Continuous smearing of Wilson Loops, *Proc. Sci.*, LATTICE2011 (2011) 249 [arXiv:1110.3522].
[140] S. Syritsyn and J. W. Negele, Oscillatory terms in the domain wall transfer matrix, *Proc. Sci.*, LATTICE2007 (2007) 078 [arXiv:0710.0425].
[141] A. Nicholson, E. Berkowitz, C. Cheng Chang, M. A. Clark, B. Joo, T. Kurth, E. Rinaldi, B. Tiburzi, P. Vranas, and A. Walker-Loud, Neutrinoless double beta decay from lattice QCD, *Proc. Sci.*, LATTICE2016 (2016) 017 [arXiv:1608.04793].
[142] C. Bouchard, C. Cheng Chang, T. Kurth, K. Orginos, and A. Walker-Loud, On the Feynman-Hellmann theorem in quantum field theory and the calculation of matrix elements, Phys. Rev. D **96**, 014504 (2017).
[143] E. Berkowitz *et al.*, An accurate calculation of the nucleon axial charge with lattice QCD, arXiv:1704.01114.
[144] S. Basak, R. G. Edwards, G. T. Fleming, U. M. Heller, C. Morningstar, D. Richards, I. Sato, and S. Wallace, Group-theoretical construction of extended baryon operators in lattice QCD, Phys. Rev. D **72**, 094506 (2005).
[145] S. Basak, R. Edwards, G. T. Fleming, U. M. Heller, C. Morningstar, D. Richards, I. Sato, and S. J. Wallace (LHPC Collaboration),, Clebsch-Gordan construction of lattice interpolating fields for excited baryons, Phys. Rev. D **72**, 074501 (2005).
[146] T. Blum *et al.*, Quenched lattice QCD with domain wall fermions and the chiral limit, Phys. Rev. D **69**, 074502 (2004).
[147] Y. Aoki *et al.*, Domain wall fermions with improved gauge actions, Phys. Rev. D **69**, 074504 (2004).
[148] G. Peter Lepage, lsqfit v8.1, 2016.
[149] C. M. Bouchard, G. Peter Lepage, C. Monahan, H. Na, and J. Shigemitsu, $B_s \to K\ell\nu$ form factors from lattice QCD, Phys. Rev. D **90**, 054506 (2014).
[150] S. Borsanyi *et al.*, High-precision scale setting in lattice QCD, J. High Energy Phys. 09 (2012) 010.
[151] A. Bazavov *et al.* (MILC Collaboration), Gradient flow and scale setting on MILC HISQ ensembles, Phys. Rev. D **93**, 094510 (2016).
[152] M. Albanese *et al.* (APE Collaboration), Glueball masses and string tension in lattice QCD, Phys. Lett. B **192**, 163 (1987).
[153] C. Bernard, S. Datta, T. A. DeGrand, C. E. DeTar, S. A. Gottlieb, U. M. Heller, C. McNeile, K. Orginos, R. Sugar, and D. Toussaint (MILC Collaboration), Lattice calculation of heavy light decay constants with two flavors of dynamical quarks, Phys. Rev. D **66**, 094501 (2002).
[154] A. Frommer, B. Nockel, S. Gusken, T. Lippert, and K. Schilling, Many masses on one stroke: Economic computation of quark propagators, Int. J. Mod. Phys. C **06**, 627 (1995).
[155] J. Gasser and H. Leutwyler, Chiral perturbation theory: Expansions in the mass of the strange quark, Nucl. Phys. **B250**, 465 (1985).
[156] G. Colangelo, S. Dürr, and C. Haefeli, Finite volume effects for meson masses and decay constants, Nucl. Phys. **B721**, 136 (2005).
[157] S. Durr, Z. Fodor, C. Hoelbling, S. D. Katz, S. Krieg, T. Kurth, L. Lellouch, T. Lippert, A. Ramos, and K. K. Szabo, The ratio FK/Fpi in QCD, Phys. Rev. D **81**, 054507 (2010).

[158] A. Bazavov *et al.* (Fermilab Lattice and MILC Collaborations), $B^0_{(s)}$-mixing matrix elements from lattice QCD for the Standard Model and beyond, Phys. Rev. D **93**, 113016 (2016).

[159] H.-J. Kim and T. Izubuchi, Möbius domain wall fermion method on QUDA, *Proc. Sci.*, LATTICE2013 (2014) 033.

[160] M. A. Clark, R. Babich, K. Barros, R. C. Brower, and C. Rebbi, Solving Lattice QCD systems of equations using mixed precision solvers on GPUs, Comput. Phys. Commun. **181**, 1517 (2010).

[161] R. Babich *et al.*, Scaling Lattice QCD beyond 100 GPUs, arXiv:1109.2935.

[162] T. Blum, T. Izubuchi, and C. Jung (private communication).

[163] The HDF Group, Hierarchical Data Format, version 5, (1997-NNNN), http://www.hdfgroup.org/HDF5/.

[164] T. Kurth, A. Pochinsky, A. Sarje, S. Syritsyn, and A. Walker-Loud, High-Performance I/O: HDF5 for Lattice QCD, *Proc. Sci.*, LATTICE2014 (2015) 045 [arXiv:1501.06992].

[165] E. Berkowitz, METAQ, https://github.com/evanberkowitz/metaq, 2016.